Ana Carlota
Cação Moreira

Simulação numérica baseada em software comercial para reproduzir o comportamento eletroquímico e térmico 3D de baterias de lítio

Commercial software-based numerical simulation to reproduce the 3D electrochemical-thermal behaviour of lithium-ion batteries

Universidade de Aveiro
2022

Ana Carlota
Cação Moreira

Simulação numérica baseada em software comercial para reproduzir o comportamento eletroquímico e térmico 3D de baterias de lítio

Commercial software-based numerical simulation to reproduce the 3D electrochemical-thermal behaviour of lithium-ion batteries

Dissertação apresentada à Universidade de Aveiro para cumprimento dos requisitos necessários à obtenção do grau de Mestre em Engenharia Computacional, realizada sob a orientação científica do Doutor Carlos Alberto Ferreira Marques, Equiparado a Investigador Principal do Departamento de Física da Universidade de Aveiro, e do Doutor Micael dos Santos Nascimento, Investigador Doutorado do Departamento de Física da Universidade de Aveiro.

This work was developed within the scope of the INSTABAT project (Grant agreement ID: 955930) and the i3N project, UIDB/50025/2020 UIDP/50025/2020 LA/P/0037/2020, financed by European Union funds and from the FEDER through the COMPETE 2020 program and the FCT - Portuguese Foundation for Science and Technology.

o júri / the jury

presidente / president

Professora Doutora Teresa Maria Fernandes Rodrigues Cabral Monteiro
Professora Associada com Agregação do Departamento de Física da Universidade de Aveiro

vogais / examiners committee

Professor Doutor Paulo Sérgio de Brito André
Professor Catedrático do Instituto Superior Técnico da Universidade de Lisboa
(Arguente)

Doutor Carlos Alberto Ferreira Marques
Equiparado a Investigador Principal do Departamento de Física da Universidade de Aveiro
(Orientador)

agradecimentos / acknowledgements

I would like to thank my advisor, Doctor Carlos Alberto Ferreira Marques, for all the support, motivation, availability, patience and guidance during this year. I also want to thank my co-advisor, Doctor Micael Nascimento, for the support during the year.

I am also thankful to Vitorino Biazi Neto for the help and work in the virtual sensor development.

A special thanks to my parents and family for all the support throughout my life. Without them none of this would be possible.

I finally want to thank my colleagues and friends for all the support throughout my academic journey, in the good and bad times, and for providing me with fantastic memories that I will take with me for life.

Keywords Lithium-ion batteries, Modelling, Thermal behaviour, Electrochemical, CFD

Abstract

Nowadays the increasing awareness for environmental preservation makes finding environmentally sustainable solutions more and more important. An option to reduce the environmental impact of fossil fuels is switching to renewable energy sources, and batteries play a key role in that transition process. It is increasingly fundamental to this energy sources continue to meet the market's demands regarding performance, sustainability, and efficiency. This increase in battery dependence requires more rigorous monitoring of its functional status. The monitoring process using physical sensors can be very chemical aggressive and its installation and maintenance is expensive. A reasonable option is using virtual sensors instead. This thesis contributes to the development of a thermal virtual sensor by developing a 3D battery model. The model is developed using the softwares Siemens Battery Design Studio and StarCCM+. Their potential to model the batteries available at the laboratory is also evaluated. Electrochemical, equivalent-circuit, and thermal models are explored. The NTGP (Newman, Tiedemann, Gu, Peukert) and RCR (Resistance, Capacitive, Resistive) models are used to model the prismatic battery of choice. When compared to the given experimental results, the NTGP model proved to be the most adequate to use. For lower C-rates both models got close results to the experimental value. However, for higher C-rate the NTGP proved to be more suitable. For 2C the model got relative errors of 17.33% and 21.31% against 144.61% and 67.35% for the RCR. It was also seen the influence of the boundary condition and the importance of considering heat transfer mechanisms, as the lack of them provides unrealistic results. The tests made on the prismatic cell allowed to see the influence of the C-rate and initial temperature on the cell behaviour. When modelling the cylindrical cell, deep discharging issues occurred. Despite of that, the behaviour of the cell was the expected: the voltage does not exceed the defined range and the temperature increases during the charge and discharge procedures at higher pace when it's further from the defined ambient temperature. The simulated data was used as input data as input data to the estimation prediction algorithm based on EKF which presented good convergence to the real values.

Palavras Chave Baterias de lítio, Modelação, Comportamento térmico, Eletroquímico, DFC

Resumo

Atualmente a maior preocupação com a preservação ambiental torna encontrar soluções sustentáveis cada vez mais importante. Uma opção para reduzir o impacto ambiental dos combustíveis fosseis é mudar para fontes de energia renováveis, e as baterias têm um papel importante neste processo de transição. É cada vez mais fundamental que estas fontes de energia continuem a atender às exigências do mercado em relação a performance, sustentabilidade e eficiência. Este aumento na dependência requere uma monitorização mais rigorosa do seu estado. Este processo de monitorização através de sensores físicos pode ser muito agressivo e a sua instalação e manutenção dispendiosa. Uma opção mais viável é utilizar sensores virtuais. Esta dissertação contribui para o desenvolvimento do sensor térmico virtual através do desenvolvimento de um modelo 3D para simulação de baterias, que é desenvolvido através dos softwares Siemens Battery Design Studio e StarCCM+. O seu potencial para a modelação das baterias disponíveis no laboratório também é avaliado. Modelos eletroquímicos, de circuito equivalente e térmicos também são explorados. Os modelos NTGP *(Newman, Tiedemann, Gu, Peukert)* e RCR *(Resistance, Capacitive, Resistive)* são utilizados para modelar a bateria prismática escolhida. Quando comparados com os resultados experimentais dados, os resultados da simulação com o modelo NTGP provaram que este é o modelo mais adequado a utilizar. Para C-rates mais baixos ambos os modelos obtiveram resultados próximos do experimental. No entanto, para C-rates mais elevados o modelo NTGP mostrou ser o mais adequado. Para um C-rate de 2C o modelo obteve erros relativos de 17.33% e 21.31% em comparação com 144.61% e 67.35% do RCR. Também foi vista a influência da condição fronteira e a importância da consideração de mecanismos de transferência de calor, pois a sua falta causa resultados surrealísticos. Os testes feitos para a bateria prismática permitiram notar a influencia do C-rate e temperatura inicial no seu comportamento. Quanto à modelação da bateria cilíndrica, apesar dos problemas de *deep discharching* o seu comportamento foi o esperado: a voltagem não excedeu o intervalo definido e a temperatura aumenta durante os processos de carga e descarga a um ritmo mais elevado quando está mais longe da temperatura ambiente definida. Os dados obtidos para a bateria prismática são depois utilizados como input do algoritmo de estimação baseado em EKF que apresentou boa convergência para os valores reais.

Contents

List of Figures

List of Tables

List of Acronyms

EV	Electrical Vehicle
EVs	Electrical Vehicles
HEVs	Hybrid Electrical Vehicles
PHEVs	Plug-in Hybrid Electrical Vehicles
BEVs	Battery Electrical Vehicles
LIB	Lithium-Ion Battery
SoC	State of Charge
SoX	States of Charge, Health, Power, Energy and Safety
OCV	Open Circuit Voltage
BMS	Battery Management System
BTMS	Battery Thermal Management System
FEC	Final Energy Consumption
QRL	Quality, Reliability, Life
NTGP	Newman, Tiedemann, Gu, Peukert
RCR	Resistance, Capacitive, Resistive
BDS	Battery design studio
CFD	Computational Fluid Dynamics
LCO	Lithium-cobalt oxide
NMC	Lithium Nickel Manganese Cobalt Oxide
NCA	Lithium Nickel Cobalt Aluminum Oxide
LTO	Lithium Titanate
SEI	Solid Electrolyte Interface
$LiPF_6$	lithium hexafluorophosphate
$LibF_4$	lithium tetrafluoroboratee
$LiClO_4$	lithium perchlorate
PC	propylene carbonate
EC	ethylene carbonate
DEC	diethyl carbonate
EMC	ethyl methyl carbonate
DMC	dimethylene carbonate
ECM	Equivelent circuit modelling
DFN	Doyle-Fuller-Newman
EKF	Extended Kalman Filter

CHAPTER 1

Introduction

Nowadays there is an increasing awareness for environmental preservation. As time goes on, finding environmentally sustainable solutions becomes more and more important.

Since the metropolitan regions and populations are growing [1], there is a ongoing rise in global energy consumption. According to Eurostat data the EU's final energy consumption (FEC) fell by 8% between 2019 and 2020 [2]. Although there was a reduction of 13% in the energy consumption of the transport sector in 2020 compared to 2019 levels, mainly due to the mobility restrictions imposed due to the COVID-19 pandemic, this sector's consumption had been increasing consecutively for the past 7 years [3], being the sector with the bigger percentage of FEC during the past decade, as seen on Figure 1.1 [4]. According to recent COP21, COP25, COP26 conferences, and EU2030 targets, significant CO_2 and greenhouse gas emissions reductions are necessary in a limited time period, aiming the decreasing of climate warming in 1.5-2.0 °C by 2030 [5].

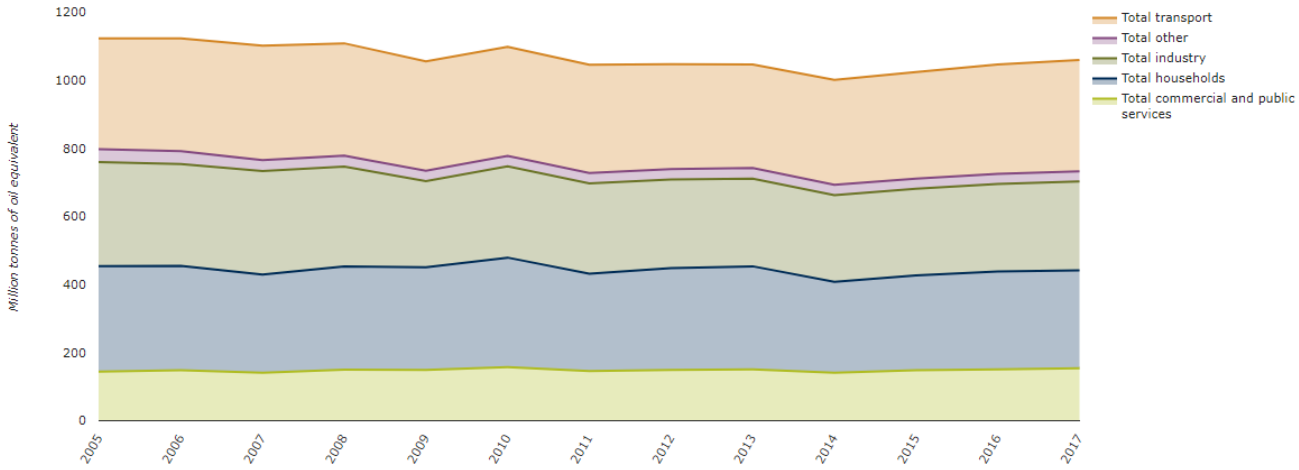

Figure 1.1: Final Energy Consumption by sector. Energy from electricity, natural gas, oil and petroleum products (excluding biofuel portion), and solid fossil fuels [4].

One way to reduce the environmental impact of fossil fuels is switching to renewable energy sources. According to the analysis from the EU Battery 2030+ large-scale research initiative

[6], batteries play a key role in this transition process, being important facilitators for the decarbonisation of both the transport and power sector. One of the most demanding points for the industry is that these energy sources, such as batteries, continue to meet the current market demands regarding performance, sustainability and efficiency [7]. With the global acceptance of Electrical Vehicles joined with this new era of connected devices, providing battery reliability, lifetime, and sustainability is becoming fundamental [8]. This increase on battery dependence requires more rigorous monitoring of the battery functional status in order to increase their quality, reliability, and life (QRL) [6].

This idea is in accordance with the INSTABAT (Innovative physical/virtual sensor platform for battery cell) objectives and ambition, which is to monitor in operando key parameters of a LIB cell, in order to provide higher accuracy SoC cell indicators, and thus allowing to improve the safety and QRL of batteries. To accomplish this goal, INSTABAT will create a proof of concept of a multi-sensor platform ("lab-on-a-cell") with integrated smart sensing technologies and functions with the capability of reliably perform in operando monitoring of the parameters mentioned above and correlating their evolution with battery cell physico-chemical degradation processes, using four embedded physical sensors and two virtual sensors based on electro-chemical and thermal reduced models [9]. Monitoring the temperature inside the battery using only physical sensors is hard to perform, as a consequence of the high chemical aggressiveness and presence of electrical noise in the environment [10]. In addition, the installation and maintenance of physical sensors increases the cost. A reasonable option to replace the physical sensors are virtual sensors.

1.1 Justification

This project contributes to the thermal virtual sensor development. Current Battery Management System (BMS) measure externally accessible parameters such as current, voltage and temperature to ensure safe operation. Nonetheless in order to allow a better control of the battery by the BMS and consequently an increased QRL and safety, internally accessible parameters could be monitored. To real-time monitor the internal state of the cell more information is needed (such as States of Charge, Health, Power, Energy and Safety (SoX)) to calculate accurate cell indicators. Improving this calculation's accuracy would allow the BMS to better control the battery cells. Despite having advancement towards instrumental miniaturisation, as well non-disturbance and compatibility with cell internal environment, through the years, there is still a long way to completely monitoring batteries in "real life". An interesting approach could also come from the use of a reduced set of measurements combined with virtual sensors to estimate other internal variables.

Despite the advancement of thermal sensing elements and their positioning strategies [11], the most demanding challenge has been to localise with accuracy the hottest spots in the battery. Algorithms for thermal virtual sensors based on thermal models [12] use battery characteristic parameters, which are estimated using the "prediction error minimisation" method and can be combined with a Kalman filter algorithm [13]–[15].

With the virtual sensor as a goal, a thermal cell 3D model will be developed. LIB cell electrical and thermal modelling can be done following different paths. In the first approach all chemical exothermic and endothermic reactions are taken into account to model temperature and potential variations and in the second empirical or electric equivalent models are based on experimental data measurement acquisitions. Both options are time dependent but do not require to be spatially solved. Nevertheless, battery modelling is a spatial problem and must be solved in 3D computation [16]. The chosen softwares in this work were the Siemens Battery design studio and StarCCM+. Another objective is to evaluate the software's potential to be used as a simulation tool to model the batteries available at the laboratory.

1.2 Outline of work

This thesis is structured as follows:

- The current chapter gives an introduction to the work and its motivations, as well as the goals set to develop it.
- Chapter 2 provides a more in depth explanation of the important concepts needed to do the work. The types of electrical vehicles, the LIB working principals, materials, thermal management and battery modelling are described. The latter includes electrochemical, equivalent-circuit and thermal modelling. The NTGP and RCR models are better explored as they are being implemented in the practical part of the work.
- Computational modelling is explored in chapter 3. After a brief description of this tool and introduction to the software used in the work, the batteries of choice for this thesis are presented, followed by the procedures for both BDS and StarCCM+ models.
- Chapter 4 consists of the results and discussion. Here a comparison of the models used is done, the results of the preformed tests for the development of the thermal virtual sensor are presented and the challenges of modelling different types of batteries are discussed.
- Chapter 5 contains information about the thermal virtual sensor development. Here a T-BASE algorithm that uses the results presented in the previous chapter as input data is presented, as well as some of the results of its implementation.
- Lastly, in chapter 6 there are the conclusions and future work. Here are the overall thoughts about the work done and possible steps to take to optimize and continue the work in the future.

CHAPTER 2

Fundamentals

2.1 Electrical Vehicles

As mentioned in chapter 1, the transport sector is the main contributor to EU's FEC. In this sector, one way to reduce the impact of fossil fuels is switching to more environment-friendly transportation such as Electrical Vehicles (EVs), and improve their quality and efficiency.

Hybrid Electrical Vehicles (HEVs) are the initial stage in this switch. In theory, they have two different energy sources: an internal combustion engine (ICE) that uses mostly gasoline or diesel, and an electric motor usually powered by a battery. The electric motor offers energy recovery to the system when braking, and additional power to the ICE, reducing its size and power. This helps reducing the fuel consumption and emissions [17]. Depending on the level of hybridization, various hybrid types are developed, including the Micro-HEVs, the Mild-HEVs, the Full-Hybrid and the Plug-in Hybrid Electrical Vehicles (PHEVs). The latter are based on the other types of HEVs, and usually require high capacity batteries that are able to store sufficient electricity to reduce the use of petroleum [17]. Battery Electrical Vehicles (BEVs) are powered only by electricity and are becoming more popular with the improvement of battery technology. These vehicles are more efficient than HEVs ad PHEVs.

2.2 Lithium-ion batteries

In what regards to powering environment-friendly transportation an important requirement is that the batteries that do so can output a lot of power while having a long life cycle, low price and with the best efficiency possible. LIB seem to be the ones that fill this requirement the most due to its higher energy density, power capabilities, lowest reduction voltage and low atomic mass in comparison to other battery technologies [17] [18]. Figure 2.1 shows the relation between various types of secondary batteries in a Ragone plot considering its specific power and specific energy [19].

Despite of their advantages, LIB cells have some drawbacks compared to other types of rechargeable cells. They are not as robust as some other cells so protection circuits are

required to maintain the voltage and current within safe limits, and are subject to aging even when not in use.

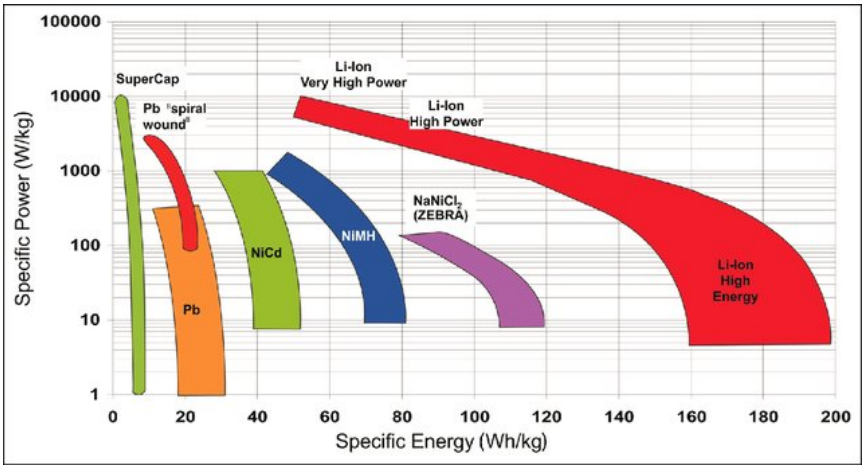

Figure 2.1: Specific energy and specific power of different battery types [19].

On figure 2.2 are presented the multiple LIB cell design concepts: cylindrical, prismatic and pouch. Cylindrical cells design gives them a strong mechanical resistance to external shocks and pressure from the outside at a reduce production cost. The low packing density gives these cells lower energy density, but provides more effective compelling options. Prismatic cells have more packaging efficiency, but thermal management is more challenging and are more expose to damage from the outside environment. Pouch cells do not have a rigid case, which provides a higher energy density but makes the cell more exposed to impact [20].

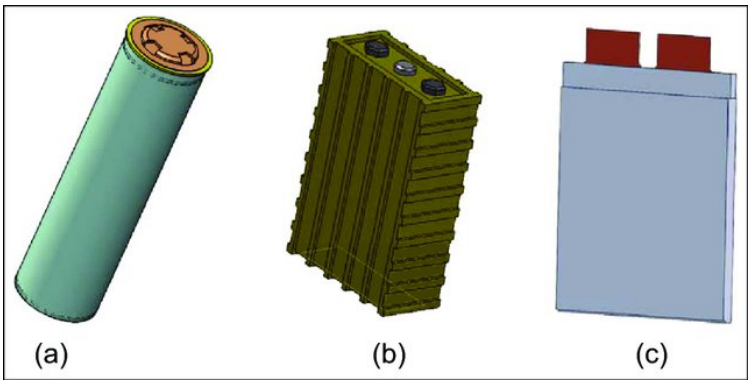

Figure 2.2: Various LIB cell designs: (a) cylindrical; (b) prismatic; (c) pouch [19].

LIB have four main components: two electrodes (the anode and the cathode), an electrolyte and a separator. The electrodes work as electrons receiver and transmitter, the electrolyte serves as the active electrical material that enables the electrons flux inside the battery and the separator separates both halves of the battery so it does not short-circuit [18].

The working principle of LIB is illustrated on figure 2.3. Basically, during the charging of the battery (when an external load is applied) lithium-ions are extracted from the cathode into the anode migrating via the electrolyte. During the discharging the reverse process occurs.

Some of the most important features of the battery are [18]:

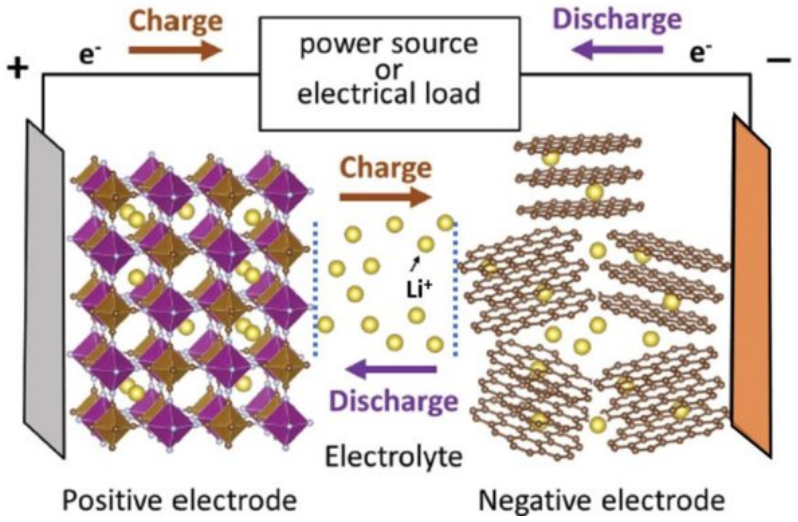

Figure 2.3: Illustration of the working principle of LIB [21].

- Nominal voltage - It represents the manufacturer recommended voltage. It can also be called the operating voltage and lies between the maximum and cut-off voltages;
- Maximum voltage – It defines the voltage over which the battery cannot be charged, according to the manufacturer. Charging it above this value may cause the battery to stop working;
- Cut-off voltage - It is the battery threshold, below which the battery cannot be discharged, according to the manufacturer. Discharging it below this voltage may cause the battery to stop functioning;
- Capacity – It defines the energy stored inside the battery cell and it is expressed in Ah. For example, a battery with a 1 Ah has enough energy stored, when fully charged, to supply 1 A during one hour. This value also defines the current discharge for the various continuous discharge rates.
- SoC - It defines how much a battery capacity is still left after a certain procedure (charge or discharge) in a certain time period;
- C-rate - It is a measurement of how much the battery is charging or discharging. It is given by the amount of energy that the battery will theoretically provide in a hour. For example, at 1C, the battery will be fully discharge in one hour, at 2C in half an hour, and at 4C in 15 minutes, and so on.

2.2.1 Cathode material

The cathode stores the lithium ions. The most common materials used for the positive electrode are listed bellow [22], [23]:

- Lithium-cobalt oxide ($LiCoO_2$ or LCO): the most common cathode material and widely used in portable applications. LCO is a particularly dense material and provides a high energy density. However, it is relatively expensive and its structural instability raises some safety issues.

- Lithium Iron Phosphate ($LiFePO_4$ or LFP): this material provides exceptional safety and a long life span. However, compared to other LIB they provide a moderate specific energy and a lower voltage.
- Lithium Manganese Oxide ($LiMn_2O_4$ or LMO): this material forms a three-dimensional spinel structure that enhances ion flow on the electrode. This structure also has high thermal stability and provides a low internal cell resistance, which allows fast charging and high-current discharging. However, compared to LCO, this material has a more moderate specific energy and the its cycle and calendar life are restrained.
- Lithium Nickel Manganese Cobalt Oxide ($LiNi_xMn_yCo_zO_2$ or NMC): the preferred type for EVs. NMC has a great overall performance and excels on specific energy. Due to the presence of Manganese (Mn), the NMC batteries are less expensive compared to LCO and NCA.
- Lithium Nickel Cobalt Aluminum Oxide ($LiNi_xCo_yAl_zO_2$ or NCA): this material has a satisfying rate capability and energy density, and due to its limited cobalt content is potentially low-cost. NCA is mostly used in high-capacity consumer cells and some EVs.

2.2.2 Anode material

As mentioned, during discharge the lithium ions migrate from the cathode to the anode. The most common materials used for the negative electrode are listed bellow:

- Graphite: its high specific capacity makes it one of the most common anode materials [24]. The layers of tightly bonded C6 structures that make the graphite can only accommodate one lithium atom for every six carbon ones. This low lithium insertion potential causes the deposition of metallic lithium on the surface of the anode. Another drawback of this material is the poor performance at low temperature and the formation of a Solid Electrolyte Interface (SEI) [25].
- Lithium Titanate (LTO) [26], [27]: its higher insertion potential makes it a better insertion material. This material makes the battery more safe and lasting because the electrolyete is more stable and Solid Electrolyte Interface less favorable. However, it has a lower specific capacity, therefore the batteries have low energy density. Batteries with LTO anode have lower voltage, as a consequence of the high anode potential.

2.2.3 Electrolyte

The electrolyte provides a conductive pathway for lithium ions to move from electrode to electrode during charge and discharge.

A larger ionic conductivity, a stabilized evolution of the SEI and a higher thermal and electrical stability are some of the requirements that should be fulfilled by the electrolyte [28]. As lithium reacts violently with water, the electrolyte is composed of a non-aqueous organic solvents plus a lithium salt. Because of its higher ionic conductivity, the most commonly used lithium salt is lithium hexafluorophosphate ($LiPF_6$), but lithium tetrafluoroboratee ($LibF_4$), lithium perchlorate ($LiClO_4$), and several others can be used. $LiPF_6$ is frequently dissolved on carbonate-based aprotic solvents such as propylene carbonate (PC), ethylene carbonate (EC),

diethyl carbonate (DEC), ethyl methyl carbonate (EMC) or dimethylene carbonate (DMC) [17].

2.2.4 Separator

The separator is a microporous material whose main purpose is being an electronic insulator to avoid contact between the cathode and anode while permitting ionic transport. It also has the "shutdown" function, where the separator ceases to allow ionic transport at high temperatures for safety. To provide the numerous functions required, multi-layer separators are more frequently used. Even though the separator should not influence the cell's internal reactions, its design is crucial for the performance of the cell. Separator properties can be linked to interfacial characteristics, internal resistance, capacity, cycling, and safety of the cell. Some of these properties include: chemical stability, dimensional stability, pore structure and geometry, tortuosity, wettability, thickness, porosity, MacMullin number, and density [29]. The last four properties mentioned are allowed to be defined in BDS.

2.3 Battery Thermal management

As mentioned, lithium-ion batteries currently have and important part in what regards to powering environment-friendly transportation. They currently have higher energy density, power capabilities, lowest reduction voltage and low atomic mass in comparison to other battery technologies. However, cost, safety and temperature performance are still obstacles to its application. As known, during the charge and discharge processes occur chemical and electrochemical reactions. These reactions generate heat that accumulates inside the battery and consequently accelerates the reaction between cell components. If the temperature of the battery rises rapidly and exceeds the safe temperature range, thermal runaway can occur [17] [30]–[32]. This process is illustrated on figure 2.4.

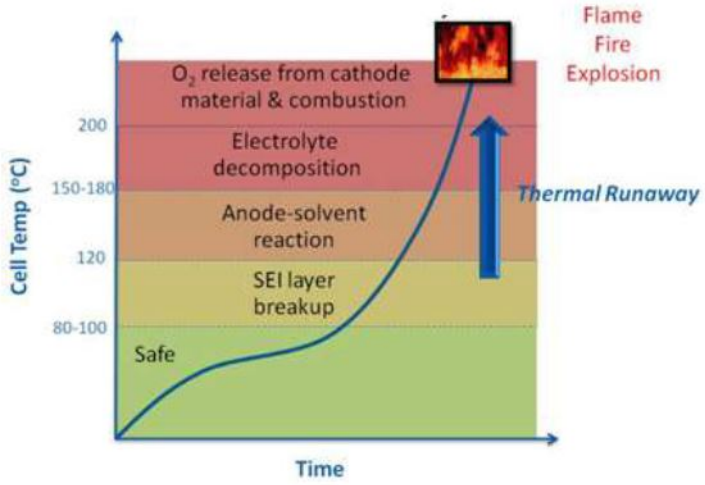

Figure 2.4: Thermal runaway process [17].

For optimal performance, safety and durability the battery need to operate respecting the defined range of voltage, current and temperature. These ranges can vary depending on the cell chemistry and the battery manufacturer [33].

Temperature has a major impact on the battery's behavior and thus, in order to regulate the operating temperature, a Battery Thermal Management System (BTMS) is needed as part of the battery system. The leading temperature extend of ambient temperature for LIB is arranged between 25 °C and 40 °C [34]. Temperatures that exceed the established boundary values have consequences that may lead to a reduction of battery performance and lifetime [35], [36]. These occurrences are briefly summed up in table 2.1.

Low temperature	Capacity drop Internal resistance increase
High temperature	Internal resistance decrease Accelerated aging phenomena Higher self-discharge Decomposition of electrolyte Thermal runaway, safety considerations Reduced life cycle

Table 2.1: Influence of temperature on working principle of batteries: global trends [34].

2.4 Battery Modelling

2.4.1 Electrochemical Modelling

Electrochemical models provide a fundamental insight of the internal mechanisms of the battery. Most of these types of models arise from the Doyle-Fuller-Newman (DFN) model [37], which is based on the porous electrode and concentrated solution theory [38]. As shown in figure 2.5, the battery is composed by two electrodes and one separator region, and the electrodes are considered a sum of indistinguishable spheres particles. By using multiple partial differential equations all the chemical reactions and dynamics of the battery are described.

These models demonstrate a clear relationship between the electrochemical parameters and battery geometry, making them more appropriate to study battery designs. Another advantage is their high accuracy. However, it can be challenging obtaining the required parameters and major computational power is required [17], [18].

Multiple work was been developed based on this model using numerous approaches, from simpler 1D models to 2D and 3D electrochemical-thermal models [17]. In order to minimize the need for high computational power, a simplification of the complete models is needed. With this goal, a polynomial approximation (PP model), a single particle model (SPM model), and the single particle model with electrolyte dynamics (SPMe) have all been interesting approaches [38].

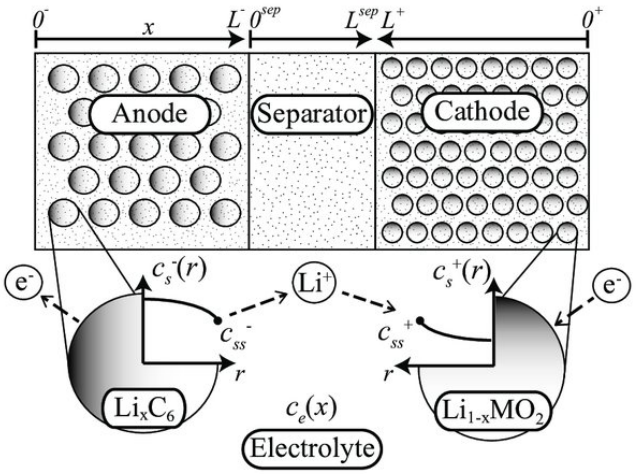

Figure 2.5: Schematic of the Doyle-Fuller-Newman model [37].

NTG Model

The NTG (Newman, Tiedemann, Gu) model [39]–[41] was developed to mathematically model current charge and discharge behavior of batteries.

The Newman, Tiedemann, Gu, Peukert (NTGP) Table model is the most recently NTG model developed and adds significant functionality over the older models. It predicts the battery's potential and temperature using constant current density along the electrodes, and also takes into account variation of current along the height and width of the electrodes and heat generation in the current collectors. The NTGP 3D table model obeys the following relation [39]–[41]:

$$V_{cell} = V(SOC_i, T) - \frac{i}{Y(SOC_i, T)} \tag{2.1}$$

For discharge:

$$SOC_i = 1 - (1 - SOC)\frac{C_{Ah-m^{-2},0}}{C_{Ah-m^{-2},1}} \tag{2.2}$$

For charge:

$$SOC_i = SOC\frac{C_{Ah-m^{-2},0}}{C_{Ah-m^{-2},1}} \tag{2.3}$$

$$SOC = \frac{\int idt}{C_{Ah-m^{-2},0}} i = \frac{I}{A} \tag{2.4}$$

$$Q = I \cdot (U_{OC} - V_{cell} - T\frac{dU}{dT}) \tag{2.5}$$

Where A is the electrode area (m^2), $C_{Ahm^{-2},0}$ the nominal cell capacity (Ahm^{-2}), $C_{Ahm^{-2},i}$ the cell capacity at current density i (Ahm^{-2}), E_a the activation energy ($Jmol^{-1}K^{-1}$), i the current density (Am^{-2}), I the current (A), SOC the state of charge, Q the electrochemical heat generation (W), T the temperature (K), U_{OC} the equilibrium voltage (V), V the Voltage term (V), V_{cell} the working cell voltage (V), and Y the admittance term ($Ohm^{-2}m^{-2}$).

2.4.2 Equivalent Circuit Modelling

Equivelent circuit modelling (ECM) is the polar oposite, being a semi-empirical model. A polynomial is done by using experimental data. It substitutes the electrochemical phenomena and converts them into electrical components, like resistances, capacitors and voltage sources in a circuit.

By negleting the electrochemical complexity the simulation becomes more simple and allows faster solving of real-life applications. The accuracy of the solution can also be incresed due to the adaptation of the circuitry of the model. However, it is challenging to accurately model the battery's physical behaviour in every situation as a consequence of them being based on data obtained in precise laboratory conditions.

Several approaches are presented in the literature, using different designs [42]–[44]. Some examples are displayed on figure 2.6.

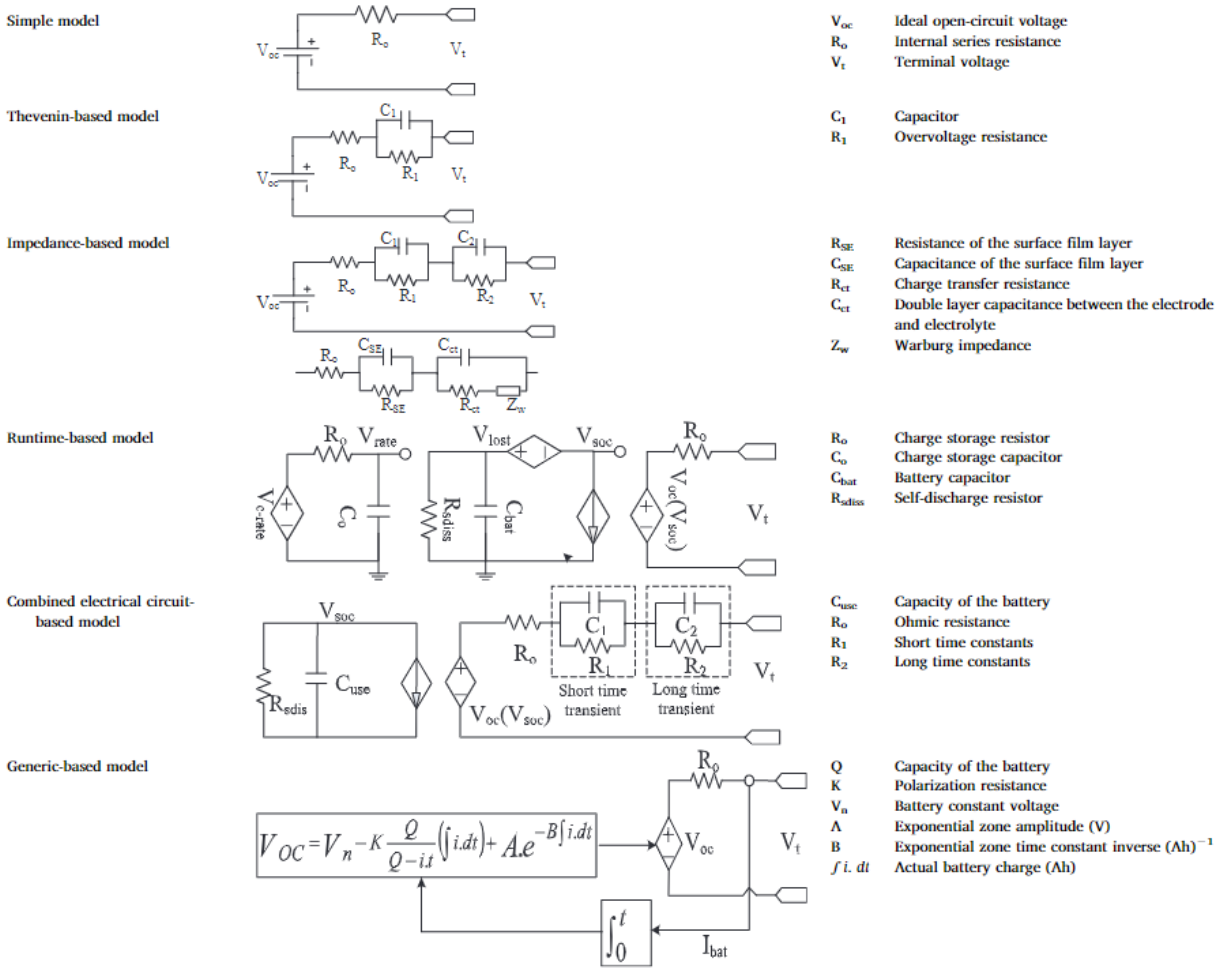

Figure 2.6: Exemples of ECM using different designs [42].

RCR Model

The Resistance, Capacitive, Resistive (RCR) models were developed to provide accurate SoC information on EV batteries. The algorithms are based on simple-circuit representation with on-line least-square regression of the parameters, and they are robust enough to provide

reasonably precise results even if mistakes have been made when specifying the initial SoC. The RCR Table model is the most recently developed [45], [46] and it is one of the models used in this thesis.

The RCR Table model for one time constant is given by [45], [46]:

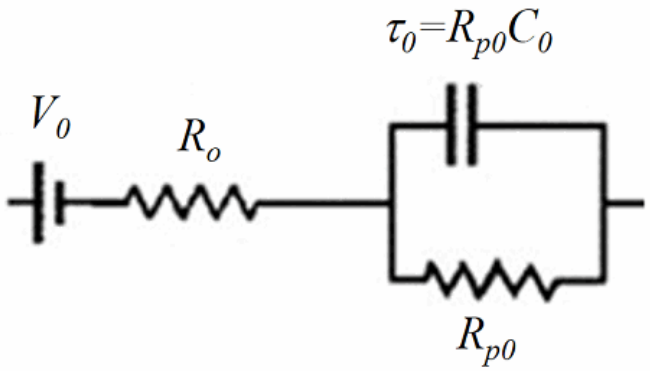

Figure 2.7: RCR table model for one time constant circuit.

$$V_L = V_0 - I \cdot R_0 - \frac{I}{C}\Delta t + (V_L - V_0 + I \cdot R_0)_{t-\Delta t} exp\left[\frac{-\Delta t}{\tau}\right] \tag{2.6}$$

Where V_0 is the zero current of open circuit voltage, V_L is the computed cell working voltage, R_0 the series resistance, R_p the polarization resistance, τ the time constant, t the time, and I the current.

In the RCR Table models, each set of V_0, R_0, R_p, and τ parameters are functions of the SoC for a particular temperature. The evolution of each parameter is specified as a table. There are no generic equations to express their evolution, as they are measured data which vary from one cell to another. In BDS, the evolution of these variables between table points is calculated by either linear interpolation or Bezier curve interpolation. These models account for the rate-dependent resistance that is found through the following relationship:

$$R_p = R_{p,0}\left(\frac{1}{\frac{|i|}{|i_1|} + exp\left(-\frac{|i|}{i_0}\right)}\right) \tag{2.7}$$

R_p being the polarization resistance which can be physically interpreted as a charge-transfer resistance. If Tafel kinetics applies, then:

$$R_p = \frac{R_{p,0}}{i} \tag{2.8}$$

However, this equation would be undefined for $i = 0$, so another term, $exp\left(-\frac{|i|}{i_0}\right)$, is added for numerical stability.

The diffusion resistance adds an additional term to the parallel resistance R_{p0}:

$$R_d = A_d\sqrt{\frac{t}{e^{B_d} - e^{V_{OC}}}} \tag{2.9}$$

Where A_d and B_d are user-specified constants, and V_{OC} is the open-circuit voltage at time t.

The polarization resistance modifies the parallel resistance R_{p0}:

$$R_{p,1} = \frac{R_{p,0}}{\frac{|i|}{|i_{p,1}|} + exp\left(-\frac{|i|}{i_{p,0}}\right)} \tag{2.10}$$

Where i is the local unit cell current density, and $i_{p,0}$ and $i_{p,1}$ are user specified constants (A/m^2).

2.4.3 Thermal Modelling

As mentioned in section 2.3, temperature has a major impact in the battery's behavior. With the goal of developing a Battery Management System, the thermal model provides the temperature distribution of the battery. One of the first works in the literature regarding battery thermal behaviour were presented by Newman and Pals, focusing on modelling a single Li-ion cell [47], and a full stack [48]. Most of the present developed models are based on the general balance model proposed by Bernardi *et al.* [49].

Thermal models take the geometry features of the battery into account, and can be developed in 1D, 2D, and 3D, having always the heat balance equation as a base:

$$\rho c_p \frac{\partial T}{\partial t} = k\nabla \cdot (\nabla T) + \dot{Q}_{generated} - \dot{Q}_{dissipated} \tag{2.11}$$

Where ρ is the battery density, c_p the specific heat, k the thermal conductivity, T the temperature, and $\dot{Q}_{generated}$ and $\dot{Q}_{dissipated}$ the generated and dissipated heat, respectively.

In what regards battery modelling, thermal and electrochemical or ECM models are often coupled. To solve these models two different approaches have been explored in the literature:

- Analytical methods, which provide continuous solutions and can clearly demonstrate how the the solutions are affected by every parameter. However, they can only be applied in less complex cases. Analytical techniques include the Laplace transformation, separations of variables, Green's function, and others [50].
- Numerical methods, which are more appropriate to solve more complex equations and, if applied correctly, have the potential to produce fairly accurate solutions. However, they can be time consuming and computationally expensive [51]. The most used numerical techniques include the finite differential method (FDM), finite volume method (FVM), and finite element method (FEM) [50]. Because of their complexity, softwares like ANSYS Fluent, COMSOL Multiphysics and StarCCM+ (used in this thesis) are usually used to implement these numerical methods.

The NTG model mentioned in section 2.4.1 considers the heat generated within the battery given by the equation [52]:

$$\rho c_p \frac{\partial T}{\partial t} = \frac{\partial}{\partial x}\left(k_x \frac{\partial T}{\partial x}\right) + \frac{\partial}{\partial y}\left(k_y \frac{\partial T}{\partial y}\right) + \frac{\partial}{\partial z}\left(k_z \frac{\partial T}{\partial z}\right) + \dot{Q} \tag{2.12}$$

Where x, y and z represent the system's axis, and $\dot{Q}$ the heat generated within the battery.

CHAPTER 3

Computational modelling

As mentioned in the previous chapter, commercial softwares are often used to implement numerical methods. The software of choice for this work is Siemens StarCCM+, a CFD based software for solving multidisciplinary problems. Its core capabilities include both fluid and solid mechanics, materials, heat transfer, turbulence, multiphase flow, motion, reacting flows, electrochemistry, electromagnetism, plasma, aeroacoustics, and computational rheology.

Regarding battery modelling, StarCCM+ is able to simulate the electrical and thermal response of a battery over the course of a load cycle. The software provides the option to simulate batteries that use either 0D or 3D cells. 0D simulations can be made entirely in StarCCM+. This option is more computationally inexpensive, has lower memory requirements, and provides more flexibility to define setting within the simulation. However, the set-up of the electric model is made manually and it generates lower fidelity results. 3D cell simulations require a .tbm output file from BDS to generate the cell geometry, electrochemical properties, and electrochemical model properties. They generate higher fidelity results, but are more computationally expensive, require higher memory requirements, and provide less flexibility to define StarCCM+ settings.

The scheme on figure 3.1 represents general simulation set-up. BDS generates a .tbm file containing the design the physical behaviour of the battery. Additionally, it's generated a .prg file that specifies the procedure to be run within the battery circuit. Both of these files are imported to StarCCM+, allowing the software to incorporate the battery physical properties, geometry, numerical models and procedure properties.

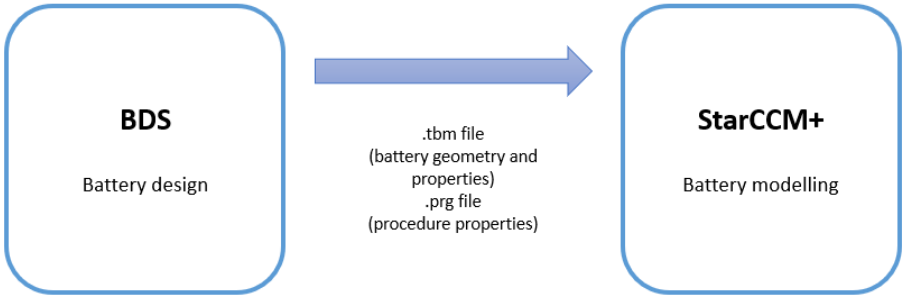

Figure 3.1: Simulation set-up scheme.

3.1 Batteries of choice for this thesis

The dimensions, cathode, anode, and electrolyte materials and some electrochemistry related properties of the chosen batteries for this thesis are show on table 3.1. More in depth details about the battery materials and properties will be explained in the next chapter.

	Battery type	Prismatic	Cylindrical
Dimensions	Lenght (mm)	67	65
	Width (mm)	50.5	—
	Thickness (mm)	3.048	—
	Diameter (mm)	—	18
Materials	Cathode	NCM-NM3100	NCM-NM3100
	Cathode current collector	Steel	Alluminuim
	Anode	Graphite	Graphite
	Anode current colector	Aluminium	Copper
	Electrolyte	LiPF6-3EC7EMC	LiPF6-3EC7EMC
Electrochemistry	Nominal cell capacity (Ah)	1.03	1.54
	Nominal voltage (V)	3.7	—
	Maximum voltage (V)	4.2	4.2
	Minimum voltage (V)	3	3.45

Table 3.1: Batteries dimensions, materials and electrochemistry properties.

3.2 Battery design studio model

BDS was used to design the chosen batteries in this work (mentioned in the previous section on table 3.1).

3.2.1 Prismatic cell

The cell was built following the steps bellow:

1. Create the cell and specify the cell type. BDS provides multiple cell templates: LiIon Simple, mostly used to design smaller cells like coin or parallel plate cells, LiIon Stack for stack cells, and LiIon Spiral for cylindrical cells. The LiIon stack cell template was chosen and can be seen on figure 3.2.

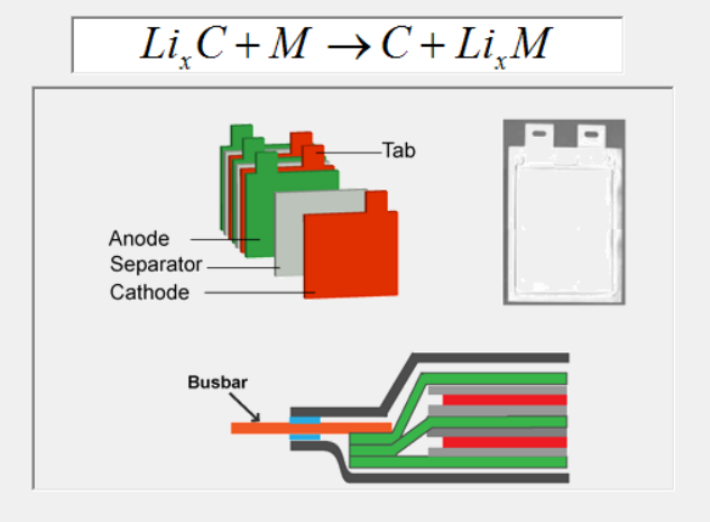

Figure 3.2: BDS stack cell template.

2. Define the electrodes' materials using the BDS data base. The positive electrode is made from NCM-NM3100 - figure 3.3 - with a steel current collector and tab - figure 3.4. The negative electrode is made from graphite - figure 3.5 - with an aluminium current collector and tab - figure 3.6. The positive and negative electrode's material tab was unknown, so it was assumed to be the same material as the respective current collectors.

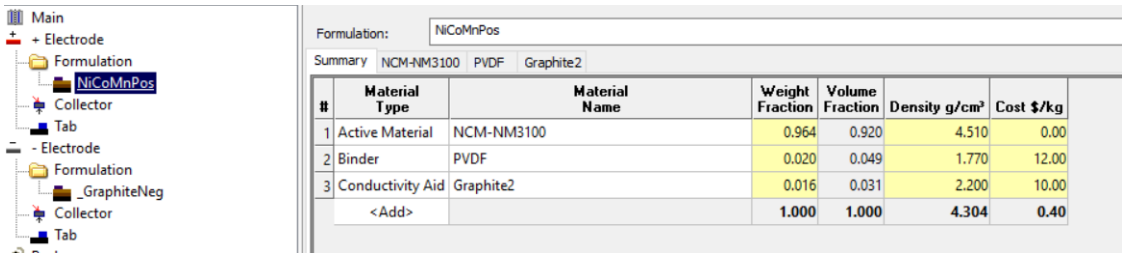

#	Material Type	Material Name	Weight Fraction	Volume Fraction	Density g/cm³	Cost $/kg
1	Active Material	NCM-NM3100	0.964	0.920	4.510	0.00
2	Binder	PVDF	0.020	0.049	1.770	12.00
3	Conductivity Aid	Graphite2	0.016	0.031	2.200	10.00
	<Add>		**1.000**	**1.000**	**4.304**	**0.40**

Figure 3.3: Prismatic cell: positive electrode properties.

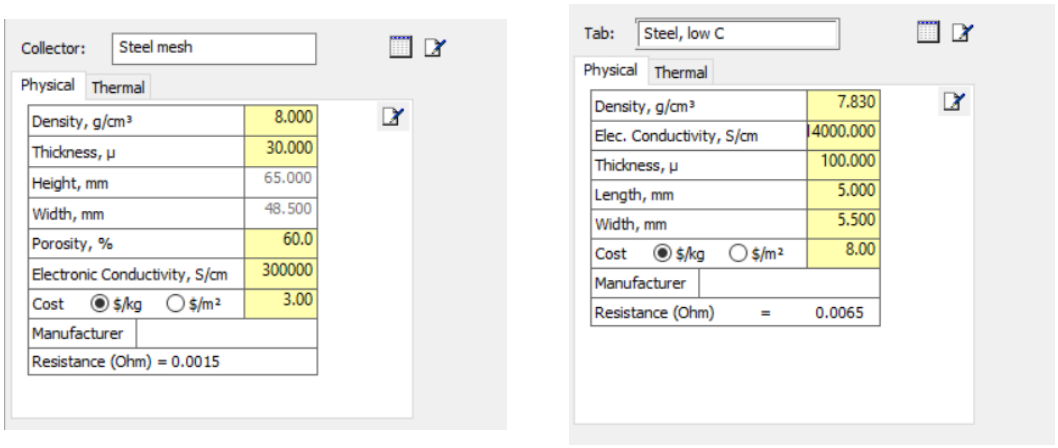

Figure 3.4: Prismatic cell: positive electrode collector (left) and tab (rigth) properties.

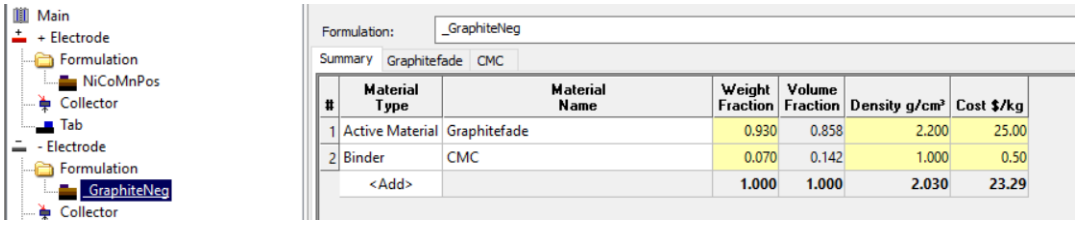

Figure 3.5: Prismatic cell: negative electrode properties.

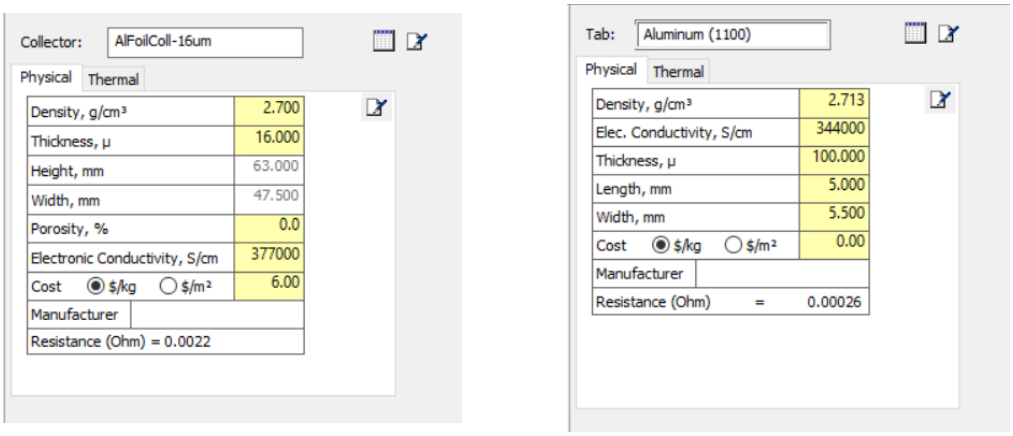

Figure 3.6: Prismatic cell: negative electrode collector (left) and tab (rigth) properties.

3. Define the electrolyte material and model. The electrolyte is composed of $LiPF6 + 2\%VC2.94 : 6.86EC/EMC$ - figure 3.7. The general electrolyte model considers the electrochemical factors that affect ion transfer in the electrolyte and it is applied to all cells within BDS.

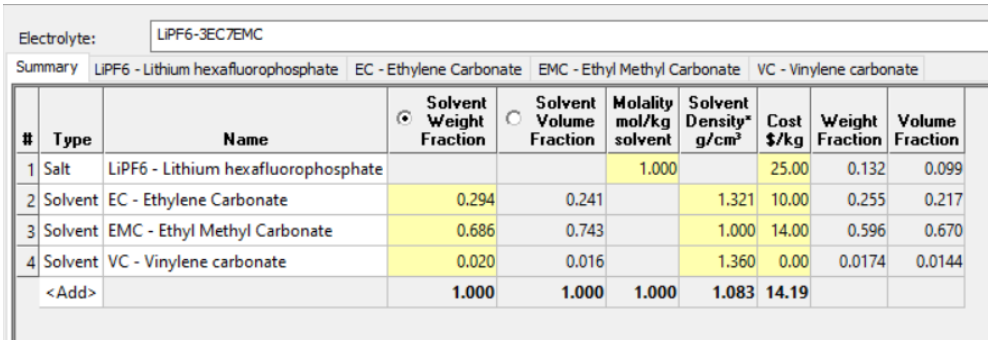

Figure 3.7: Prismatic cell: electrolytre material properties.

4. Define the cell IET (Current (I), Voltage (E), and Temperature (T)) model which models the electronic and thermal behaviour of the cell. The chosen models were the NTGTable and RCRTable, mentioned previously on sections 2.4.1 and 2.4.2.
5. Build the cell. After this step a report containing the cell, stack and electrode computed properties is generated - figure 3.8.

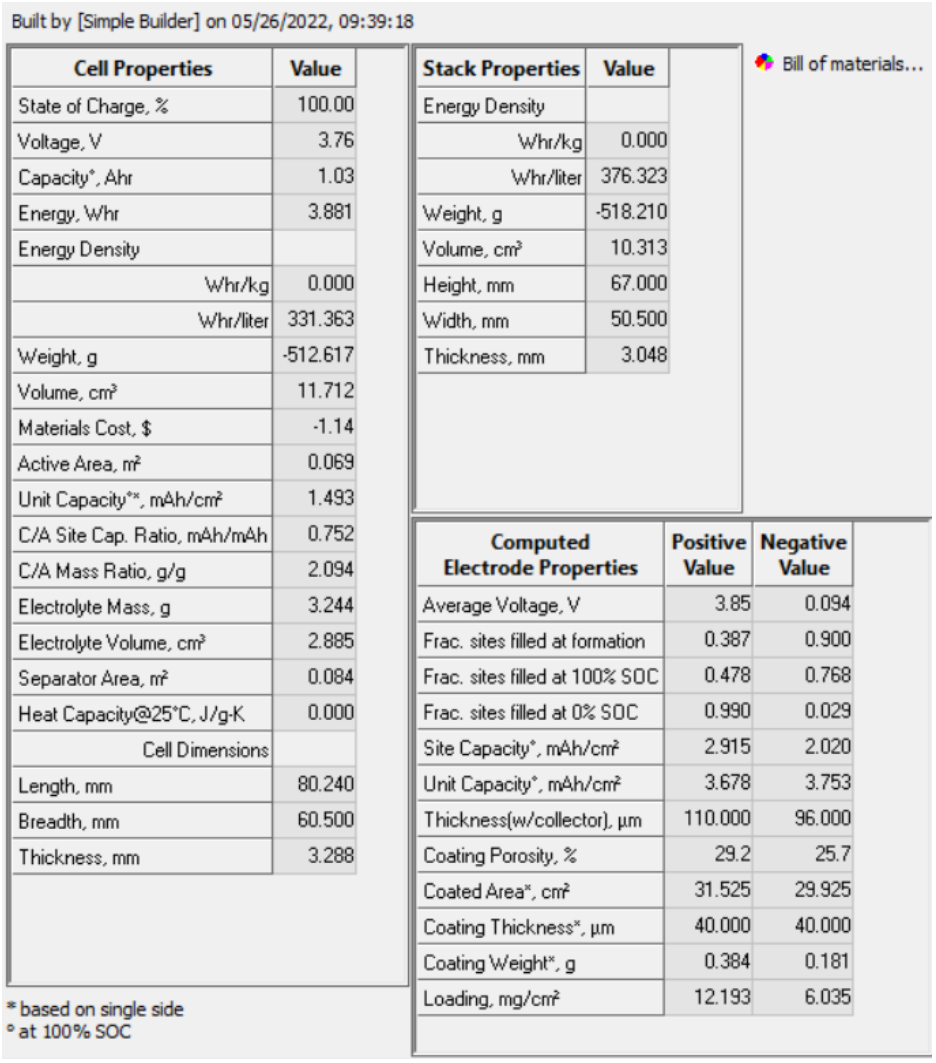

Built by [Simple Builder] on 05/26/2022, 09:39:18

Cell Properties	Value
State of Charge, %	100.00
Voltage, V	3.76
Capacity*, Ahr	1.03
Energy, Whr	3.881
Energy Density	
Whr/kg	0.000
Whr/liter	331.363
Weight, g	-512.617
Volume, cm³	11.712
Materials Cost, $	-1.14
Active Area, m²	0.069
Unit Capacity*°, mAh/cm²	1.493
C/A Site Cap. Ratio, mAh/mAh	0.752
C/A Mass Ratio, g/g	2.094
Electrolyte Mass, g	3.244
Electrolyte Volume, cm³	2.885
Separator Area, m²	0.084
Heat Capacity@25°C, J/g-K	0.000
Cell Dimensions	
Length, mm	80.240
Breadth, mm	60.500
Thickness, mm	3.288

Stack Properties	Value
Energy Density	
Whr/kg	0.000
Whr/liter	376.323
Weight, g	-518.210
Volume, cm³	10.313
Height, mm	67.000
Width, mm	50.500
Thickness, mm	3.048

Bill of materials...

Computed Electrode Properties	Positive Value	Negative Value
Average Voltage, V	3.85	0.094
Frac. sites filled at formation	0.387	0.900
Frac. sites filled at 100% SOC	0.478	0.768
Frac. sites filled at 0% SOC	0.990	0.029
Site Capacity*, mAh/cm²	2.915	2.020
Unit Capacity*, mAh/cm²	3.678	3.753
Thickness(w/collector), µm	110.000	96.000
Coating Porosity, %	29.2	25.7
Coated Area*, cm²	31.525	29.925
Coating Thickness*, µm	40.000	40.000
Coating Weight*, g	0.384	0.181
Loading, mg/cm²	12.193	6.035

* based on single side
° at 100% SOC

Figure 3.8: Prismatic cell: report of the cell, stack, and computed electrode properties.

6. Create a procedure. The creation of a procedure in BDS generates .prg file which later imported to StarCCM+ to simulate a procedure to be run within a battery circuit. The software allows the procedure type (charge, discharge, rest, end), and the type and value of the control and end condition to be defined by the user.

3.2.2 Cylindrical cell

The cylindrical cell was built following essentially the same steps as the prismatic, but with small differences regarding the cell type and electrode materials. The main differences are specified bellow:

1. Cell type. The template used was the LiIon Spiral - figure 3.9.

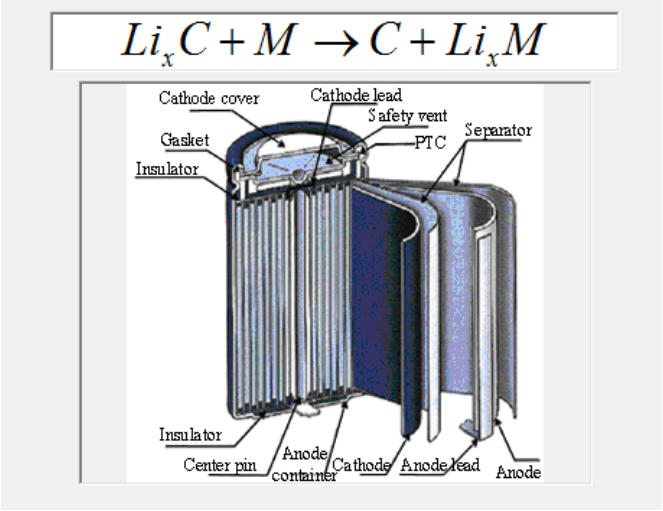

Figure 3.9: BDS spiral cell template.

2. Electrode materials. The positive electrode is made from NCM-NM3100 - figure 3.10 - with a aluminium current collector and tab - figure 3.11. The negative electrode is made from graphite - figure 3.12 - with an copper current collector and tab - figure 3.13. Like with the prismatic cell, the positive and negative electrode's tab was unknown, so it was assumed as the same material as the respective current collectors.

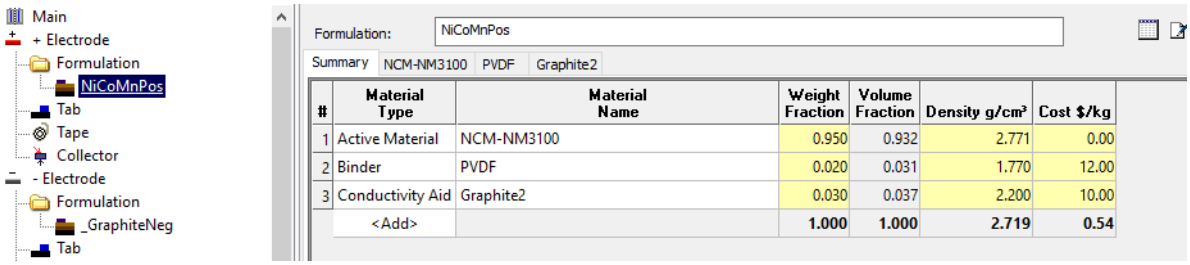

#	Material Type	Material Name	Weight Fraction	Volume Fraction	Density g/cm³	Cost $/kg
1	Active Material	NCM-NM3100	0.950	0.932	2.771	0.00
2	Binder	PVDF	0.020	0.031	1.770	12.00
3	Conductivity Aid	Graphite2	0.030	0.037	2.200	10.00
	<Add>		**1.000**	**1.000**	**2.719**	**0.54**

Figure 3.10: Cylindrical cell: positive electrode properties.

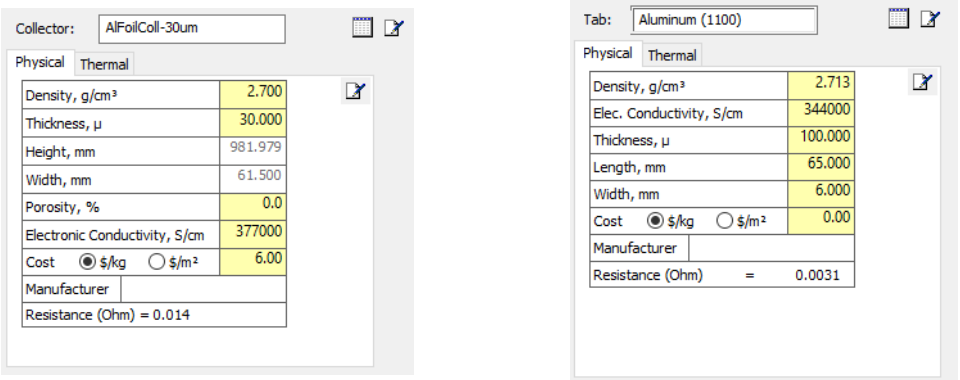

Figure 3.11: Cylindrical cell: positive electrode collector (left) and tab (rigth) properties.

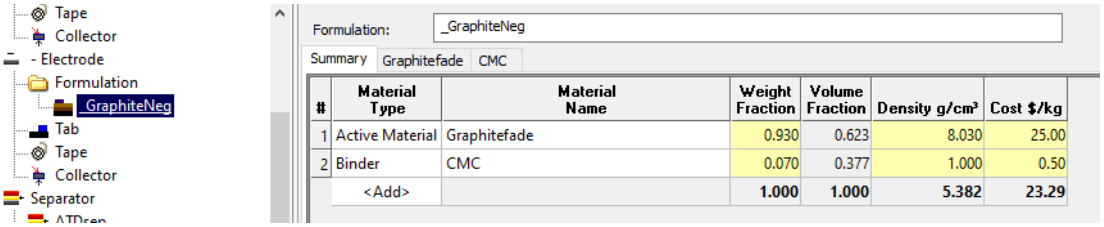

Figure 3.12: Cylindrical cell: negative electrode properties.

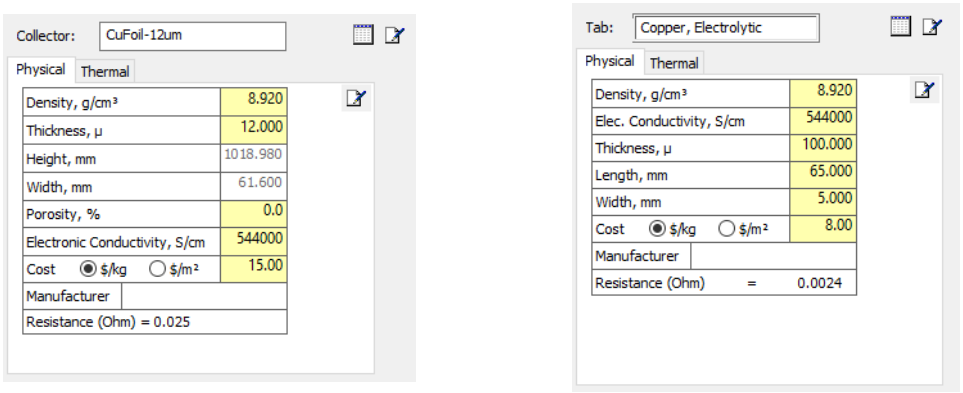

Figure 3.13: Cylindrical cell: negative electrode collector (left) and tab (rigth) properties.

3. The electrolyte is composed of $LiPF6 + 2\%VC 2.94 : 6.86 EC/EMC$ - figure 3.14.

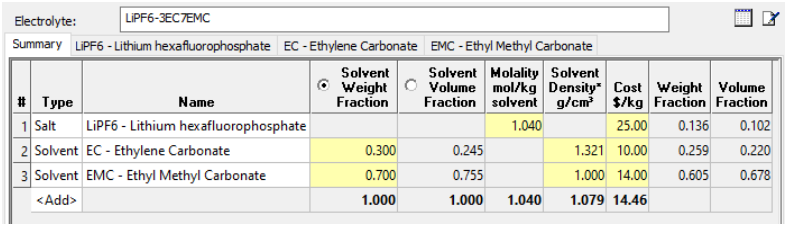

Figure 3.14: Cylindrical cell: electrolyte material properties.

The report given after building the cell is shown on figure 3.15.

Built by [Detailed Builder] on 09/21/2022, 21:10:02

Bill of materials...

View Spiral...

Cell Properties	Value
State of Charge, %	100.00
Voltage, V	3.77
Capacity*, Ahr	1.54
Energy, Whr	5.807
Energy Density	
Whr/kg	121.702
Whr/liter	351.271
Weight, g	47.717
Volume, cm³	16.532
Materials Cost, $	0.74
Active Area, m²	0.117
Unit Capacity°*, mAh/cm²	1.310
C/A Site Cap. Ratio, mAh/mAh	0.653
C/A Mass Ratio, g/g	1.815
Electrolyte Mass, g	6.206
Electrolyte Volume, cm³	5.533
Separator Area, m²	0.143
Heat Capacity@25°C, J/g-K	0.667

Jellyroll Properties	Value
Energy Density	
Whr/kg	176.451
Whr/liter	521.432
Weight, g	32.911
Volume, cm³	11.137
Height, mm	62.000
Diameter, mm	17.888

Computed Electrode Properties	Positive Value	Negative Value
Average Voltage, V	3.85	0.077
Frac. sites filled at formation	0.650	0.520
Frac. sites filled at 100% SOC	0.478	0.735
Frac. sites filled at 0% SOC	0.993	0.092
Site Capacity*, mAh/cm²	2.544	2.036
Unit Capacity*, mAh/cm²	1.329	1.497
Thickness(w/collector), µm	110.000	92.000
Coating Porosity, %	0.7	71.8
Coated Length*, cm	192.296	194.996
Coating Thickness*, µm	40.000	40.000
Coating Weight, g	12.772	7.303
Total Length, cm	98.198	101.898
Loading, mg/cm²	21.600	12.160

* based on single side at 100% SOC
° at 100% SOC

Figure 3.15: Cylindrical cell: report of the cell, stack, and computed electrode properties.

3.3 StarCCM+ model

To set up the simulation on StarCCM+ the following step were taken:

1. Set up the physics continua. On table 3.2 is a list of the selected models. The cell quality remediation and the solution interpolations are recommended in order to improve the solution accuracy. The remaining are required to use the battery module on StarCCM+. In this step is also defined the initial temperature of the battery.

Group Box	Model
Space	Three Dimensional
Material	Multi-part Solid
Time	Implicit Unsteady
Optional Models	Battery
	Circuit Model (selected automatically)
	Cell Quality Remediation
	Solution Interpolation
Energy	Segregated Solid Energy
	Gradients (selected automatically)
Equation of State	Constant Density

Table 3.2: Battery Physics

2. Define the battery cell. As mentioned, to simulate 3D cells the .tbm output file from BDS is imported. The software automatically generates the battery geometry and recognizes the cell's properties and models - figures 3.16 and 3.17.

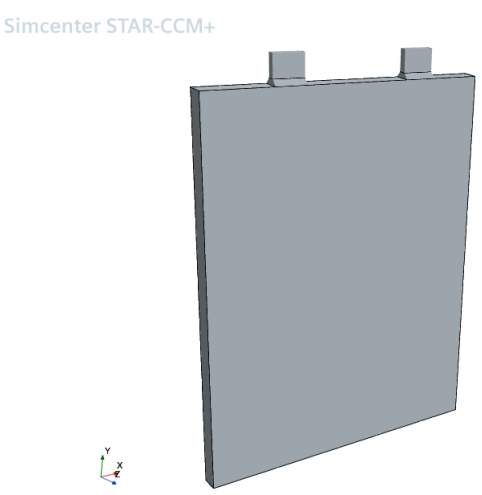

Figure 3.16: Prismatic cell: battery geometry in StarCCM+.

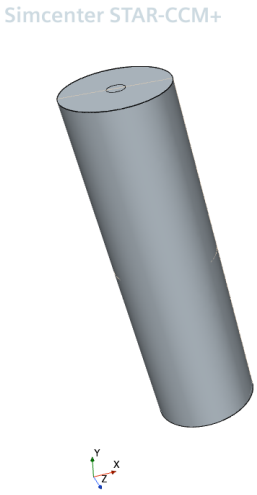

Figure 3.17: Cylindrical cell: battery geometry in StarCCM+.

3. Battery module set-up and generation of its parts.
4. Assigning the parts to regions and define the boundary conditions. Two boundary conditions for the battery walls were considered in this work. In the first simulations, the walls were considered adiabatic. Later in the process convection was introduced.
5. Create the mesh. The surface remesher, automatic surface repair, polyhedral and thin meshers were used. The battery mesh can be seen on figures 3.18 and 3.19.

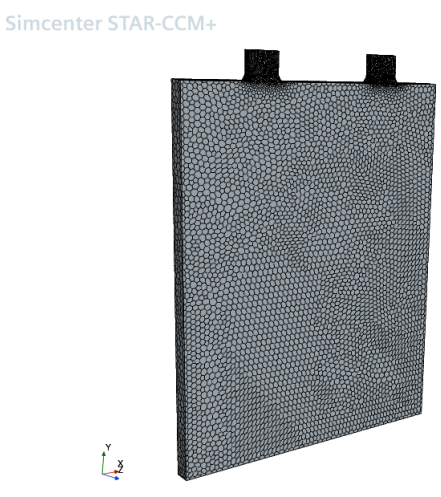

Figure 3.18: Prismatic cell: battery mesh in StarCCM+.

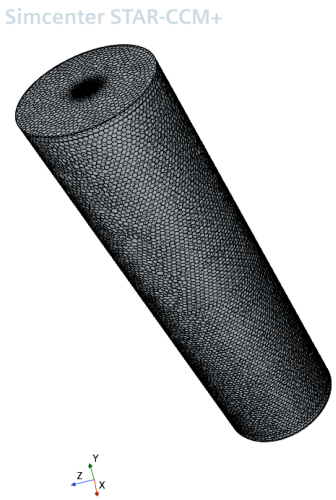

Figure 3.19: Cylindrical cell: battery mesh in StarCCM+.

6. Create the circuit. The .prg file is imported and a circuit element is created. Then connections with the battery are made and the circuit is created. The .prg file can be reloaded to update any alterations in BDS or the entire step can be repeated in the case of wanting to do a different procedure.
7. Set up the solver settings. Solvers compute the solution during the simulation run and each solver performs a specific task. Multiple solvers were used in the simulation:
    - Implicit unsteady is a time model solver. Its primary function is to control the update at each physical time for the calculation and the time-step;
    - Partitioning is responsible for controlling domain partitioning for parallel simulations. Before any physics solvers are invoked on a given global iteration or time-step, the partitioning solver is applied to ensure that the domain decomposition is up-to-date;
    - Circuit calculates the global battery voltage and current in the case of a power load, based on the voltage of each battery cell;
    - Battery;
    - Segregated Energy controls the solution update for the Segregated Fluid Energy model;
8. Post-processing step where many types of reports, monitors, plots, and scenes are created to display various outputs of the battery cell.
9. Set up the stopping criteria.
10. Run the simulation.

CHAPTER 4

Results and discussion

4.1 LIB prismatic cell

As mentioned in chapter 1, one of the goals of this work is to evaluate the software's potential to be used as a simulation tool to model the batteries at the laboratory. The properties of the prismatic cell build in BDS are briefly summarized on table 3.1 with more details on section 3.2. This battery was adapted from the one available at the laboratory and their main difference is the cathode material which was NMC622.

4.1.1 BDS model comparison

In this section the results for a type of simulation using the NTGP and RCR models will be compared. These results will be later compared to the provided experimental ones from the battery available at the laboratory.

The procedure for these simulation was a full charge cycle, followed by a 15 minute rest and a full discharge cycle. At first the simulations were made considering an adiabatic boundary condition, meaning there is no heat exchange with the environment. Although this consideration is not the most physically accurate because it does not account for any heat transfer mechanisms, it was used to simplify the simulations in a first stage and to later observe the effects of the heat transfer considerations. After that heat transfer by convection was added, considering an ambient temperature of 25 °C. All simulations were made for C/5, C/2, 1C, and 2C.

On Figure 4.2 are the given experimental results of the maximum temperature of the battery available at the laboratory for the C-rates C/5, C/2, 1C, and 2C. In the experimental set-up there were 3 different sensors in different locations within the battery to measure the temperature: ambient, surface and internal as seen on figure 4.1. More information about the acquisition of the experimental data can be found in [53]. For each C-rate the bars represent the maximum value of the battery temperature and the colors the sensor that measured it. It is seen that the highest temperature is always given by the internal sensor, so in the analysis and comparison of the models the considered temperature will be the internal. In

the StarCCM+ model this temperature was measured at the central point on the battery geometry.

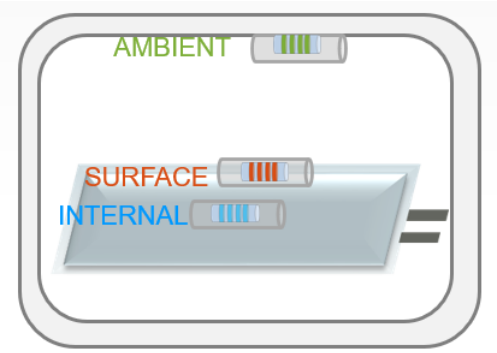

Figure 4.1: Representative scheme of the experimental location of the sensors used to measure the temperature.

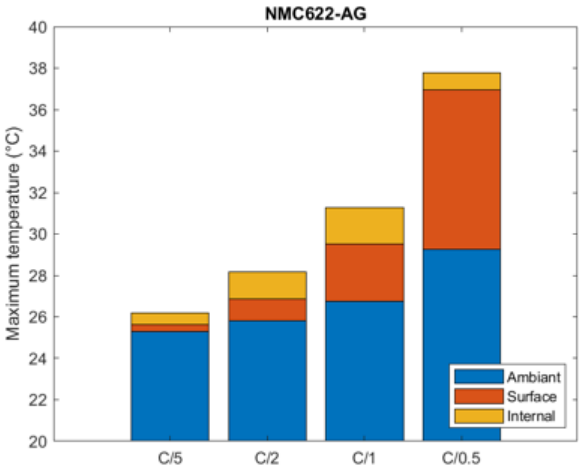

Figure 4.2: Experimental results for the maximum temperature of the battery available at the laboratory.

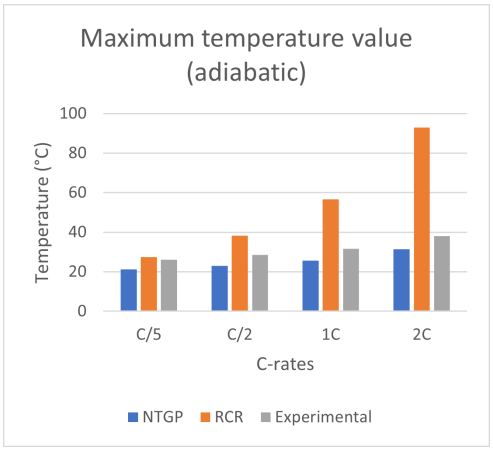

Figure 4.3: Comparison between the simulated and experimental values considering adiabatic boundary conditions with C/5, C/2, 1C and 2C.

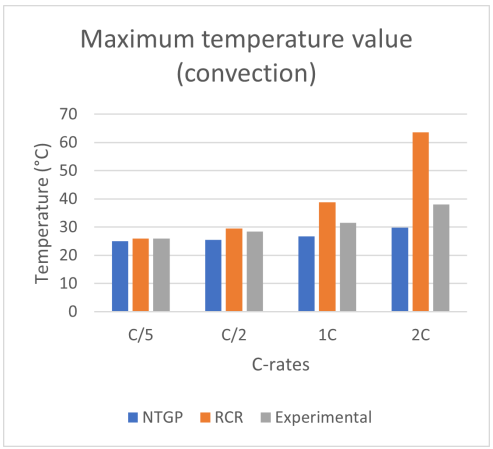

Figure 4.4: Comparison between the simulated and experimental values considering convection as a boundary condition with C/5, C/2, 1C and 2C.

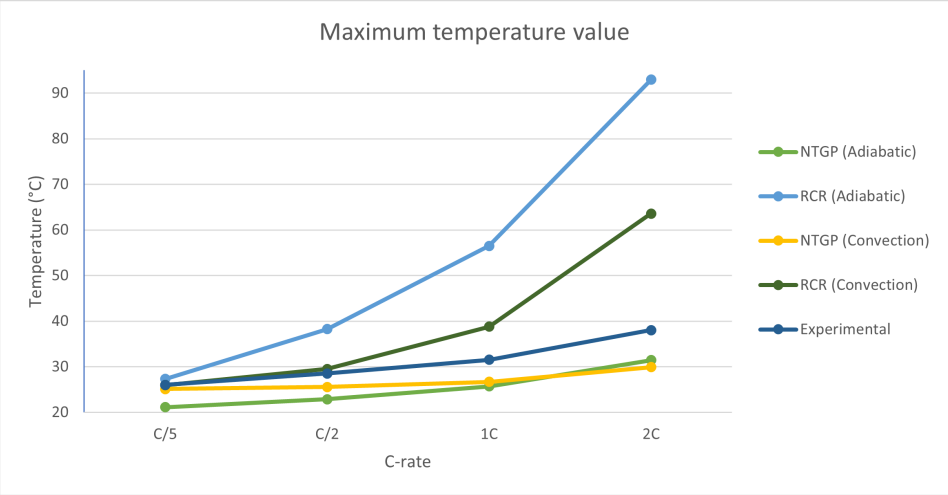

Figure 4.5: Comparison between the simulated and experimental values with C/5, C/2, 1C and 2C.

	NTGP (Adiabatic) (%)	NTGP (Convection) (%)	RCR (Adiabatic) (%)	RCR (Convection) (%)
C/5	18.69	3.48	5.02	0.2
C/2	19.81	10.39	34.24	3.58
1C	18.39	15.29	79.38	23.15
2C	17.33	21.31	144.61	67.35

Table 4.1: Relative errors for the simulated values with C/5, C/2, 1C and 2C.

Considering adiabatic boundary conditions (Figure 4.3) we can observe that for C/5 both models get maximum temperatures that are close to the experimental value, and that the RCR model gets closer results. With the increase of the C-rate the results start to diverge. The maximum temperature obtained with the RCR model increases a lot, especially for 2C, to values that are not supported by the battery. Higher current values generate more heat and because heat transfer mechanisms are not being considered, the battery overheats. On the other hand, the NTGP models gets results under the experimental value, but closer.

This small difference can happen because of the different material properties between the battery available at the laboratory and the one build on BDS. Another possible source of error may be the numerical solution of the equations which models the batteries. The huge increase in temperature from the RCR model results can happen because none of the heat transfer mechanisms are being considered.

Convection was introduced considering 25 °C as the ambient temperature and 1 W/m^2K as the heat transfer coefficient. When introducing convection (Figure 4.4) both models get a maximum temperature close to the experimental for C/5 and C/2. For 1C the difference between the simulated results is more noticeable. NTGP model gives a value under the experimental one, and RCR model gives one above. For 2C the RCR model continues to give a much higher value that expected.

Table 4.1 contains the relative errors for the simulated values for the maximum temperature. From that table and figure 4.5 it is observed that all models give better results for lower

C-rates (C/5 and C/2), having mostly the lower errors on the table. With the exception of the RCR considering adiabatic conditional, all values are under 20%. For higher C-rates (1C and 2C) the values given by the RCR model diverge more, especially without convection. The model gets bigger errors than the NTGP model, reaching values of 144.61% for 2C considering adiabatic conditions, while the highest error the NTGP model gets is 21.31% for 2C considering convection. These aspects make the RCR model less suitable for modelling this battery.

C-rate	C/5	C/2	1C	2C
Mean difference error (%)	2	9	28	70

Table 4.2: Mean difference error between the NTGP and RCR model considering convection.

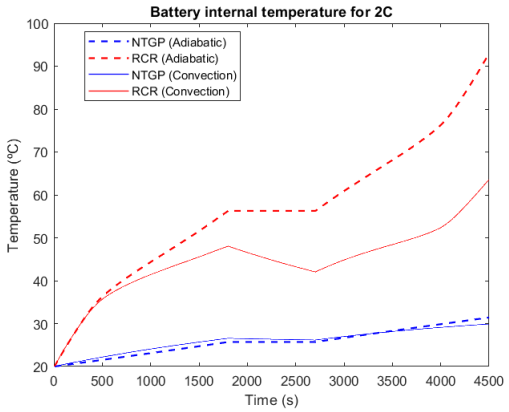

Figure 4.6: Battery internal temperature for charge and discharge cycles with 15 minute rest with 2C.

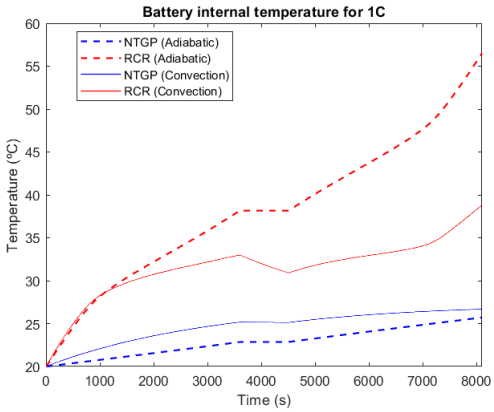

Figure 4.7: Battery internal temperature for charge and discharge cycles with 15 minute rest with 1C.

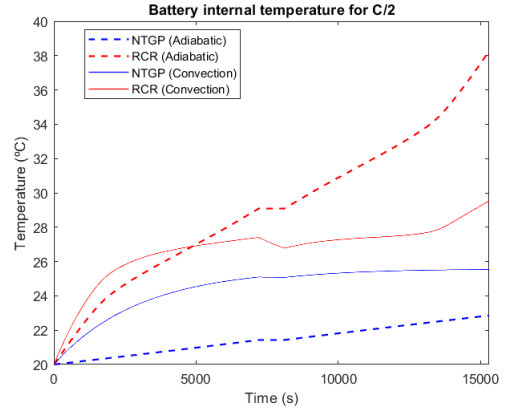

Figure 4.8: Battery internal temperature for charge and discharge cycles with 15 minute rest with C/2.

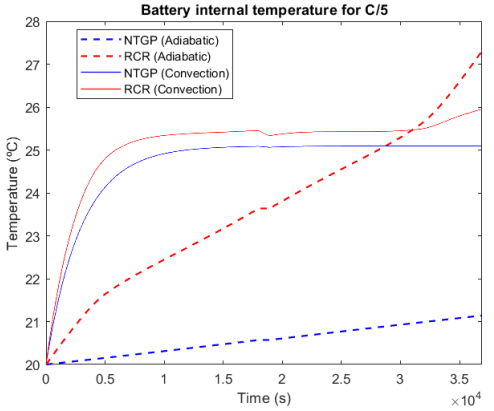

Figure 4.9: Battery internal temperature for charge and discharge cycles with 15 minute rest with C/5.

On figures 4.6, 4.7, 4.8, and 4.9 is shown the temperature of a internal center point of the battery behaviour during the procedures for 2C, 1C, C/2, and C/5, respectively.

From all the figures it can be seen that the RCR model gives higher temperatures than the NTGP. As mentioned above, it can also be observed that for the higher C-rates (2C and 1C) - Figures 4.6 and 4.7 - that the RCR model gives temperature much higher than expected, not being a suitable choice for this battery and this C-rates. It is also noticeable the differences that the introduction of convection causes: when considering some heat exchanges with the environment the battery overheat decreases. When the battery is at rest the temperature decreases due to the energy exchange with the exterior instead of staying constant.

With C/2 when considering adiabatic boundary conditions the temperature variations when increasing in charge and discharge is less noticeable because the load is smaller. Due to the smaller current with this C-rate the effects of convection are more apparent during charge and discharge: the temperature still increases but at a smaller rate when close to the ambient temperature of 25 °C. Due to the even smaller current, and consequently less heat and dissipation of energy, the temperature increases and when it reaches the ambient temperature it gets more constant. When considering adiabatic boundary conditions, it still increases but to lower values as the previous cases. Although heat dissipation does not occur with this condition, overheat does not happen because the current load is smaller. However, it would have happen for an extended simulation time.

Considering only the NTGP model, the difference between having convection or not is bigger for lower C-rates. This can be also observed on Figure 4.5.

As mentioned above, the NTGP model is the most suitable to model this battery and considering convection mechanisms is important to get more realistic results. Because of this, the mean difference errors shown on Table 4.2 is calculated considering the NTGP model as the denominator. The error increases with the C-rate, from 1.82% for C/2 to 69.96 % for 2C. This happens because the increase of the current value and the unsuitability of the RCR to model this battery.

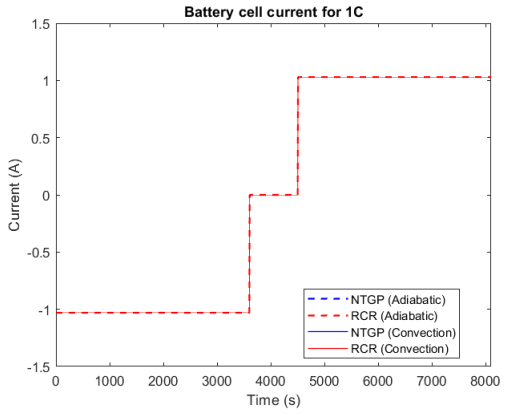

Figure 4.10: Battery cell current for charge and discharge cycles with 15 minute rest with 1C.

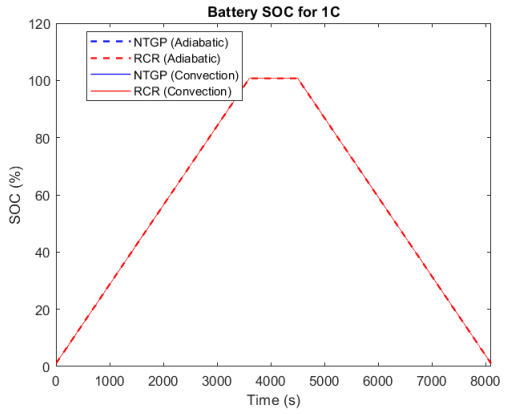

Figure 4.11: Battery SoC for charge and discharge cycles with 15 minute rest with 1C.

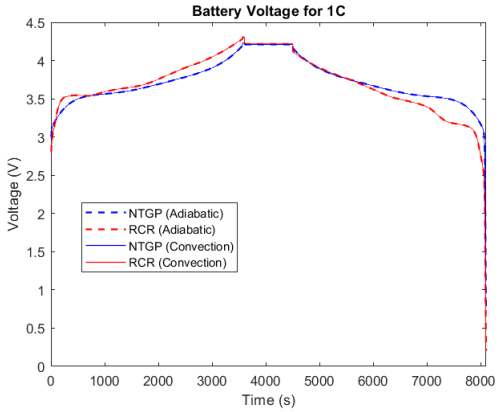

Figure 4.12: Battery voltage for charge and discharge cycles with 15 minute rest with 1C.

On Figures 4.10, 4.11, and 4.12 are the behaviour of the cell current, SoC and voltage through time during a charge, 15 minute rest, and discharge cycle with 1C respectively.

For the other 3 simulated C-rates the behaviour is very similar. During rest the current is 0A, and the absolute values for the current during charge and discharge are: 2.06 A for 2C, 0.515 A for C/2, and 0.206 A for C/5. This parameter is the same using the different models because the value of the load is defined in the procedure. Regarding the battery's SoC - all the models and boundary conditions provide similar results. For the voltage both models provide values between the same ranges, as expected. However, the behaviour between these values varies. It can also be seen that the change of the boundary condition does not influence the voltage behaviour.

4.1.2 Tests made for the thermal virtual sensor

Besides the simulations presented on the previous section, other simulations were made to be used as input data to the algorithm used in the development of the thermal virtual sensor. The tests made to obtain the results later presented in chapter 5 are summarized on Table 4.3. In addition, other tests were done:

- Charge with C/2, 1C and 2C;
- Discharge with C/2, 1C and 2C;
- Charge with 1 h rest at every 10% with C/2, 2C, and 4C;
- Discharge with 1 h rest at every 10% with C/2, 2C, and 4C;
- Charge-rest-discharge cycles with random duration and C-rates (C/2, 1C, 2C, 4C) for charge, rest, and discharge.

Procedures	Boundary condition	C-rate	Initial condition (temperature) (°C)
Discharge with 1 h rest at every 10%	Adiabatic	1C	10
			20
			40
	Convection		10
			20
			40
Charge with 1 h rest at every 10%	Convection	1C	10
			20
			40
Charge-Rest-Discharge Cycles with 1 h rest	Convection	1C	10
			20
			40
Charge-Rest-Discharge Cycles with random durations for charge, rest, and discharge	Convection	C/2	20
		1C	
		2C	

Table 4.3: Tests made to obtain the input data for the EKF based prediction algorithm.

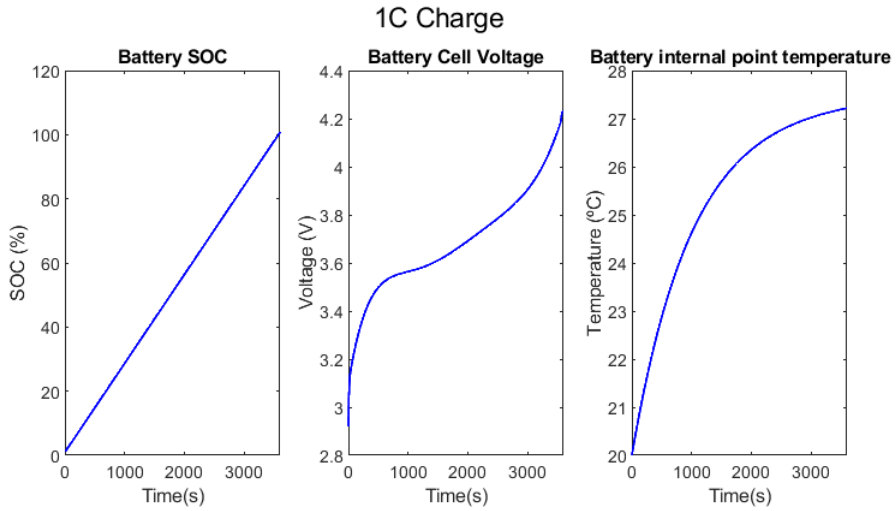

Figure 4.13: SoC, voltage, and internal temperature during a 1C charge cycle.

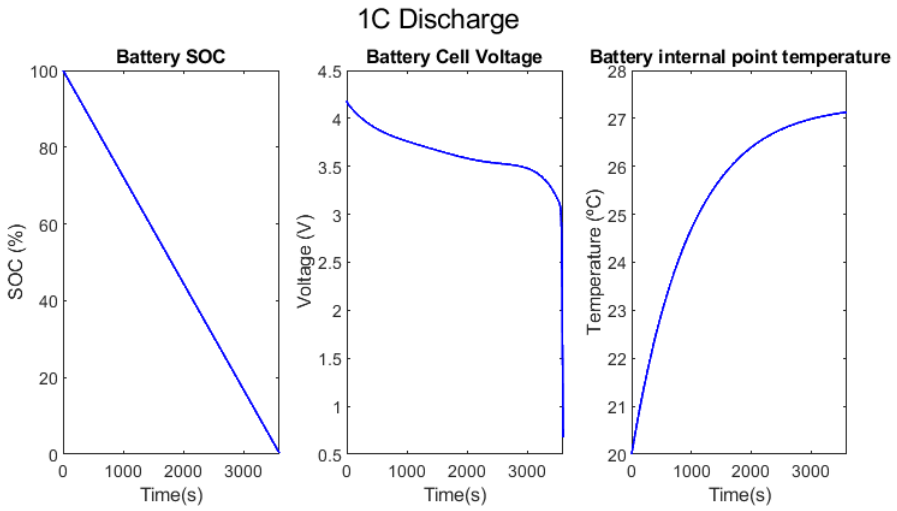

Figure 4.14: SoC, voltage, and internal temperature during a 1C discharge cycle.

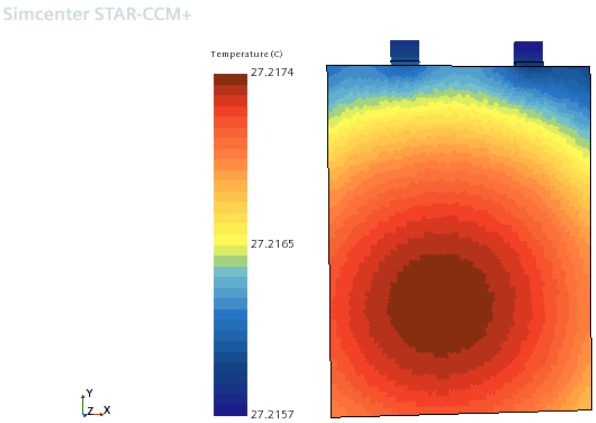

Figure 4.15: Temperature profile of the battery after a 1C charge.

On Figures 4.13 and 4.14 are the battery's SoC, voltage, and internal point temperature during a 1C charge and discharge, respectively. Both Figures show the expected behaviour of the battery: the SoC varies between 0% and 100%, the voltage is in the defined battery range (except in the last instant of discharge) and the battery temperature increases during the procedure at a higher pace when it's further from the defined ambient temperature of 25 °C.

On Figure 4.15 is shown the temperature profile of the battery after a 1C charge procedure. The temperature profile is as expected. From the figure it is seen that the higher temperature is in the stack of the battery and cathode has higher temperature than the anode which is where the current load is applied. Although the temperature value considered for the studies in the previous section is measured in a central point of the battery to mimic the location of the sensor in the experimental environment, the hot-spot does not happen in that point, occurring left and down of the central point. This can be explained by the proximity to the positive electrode and by the effect of gravity.

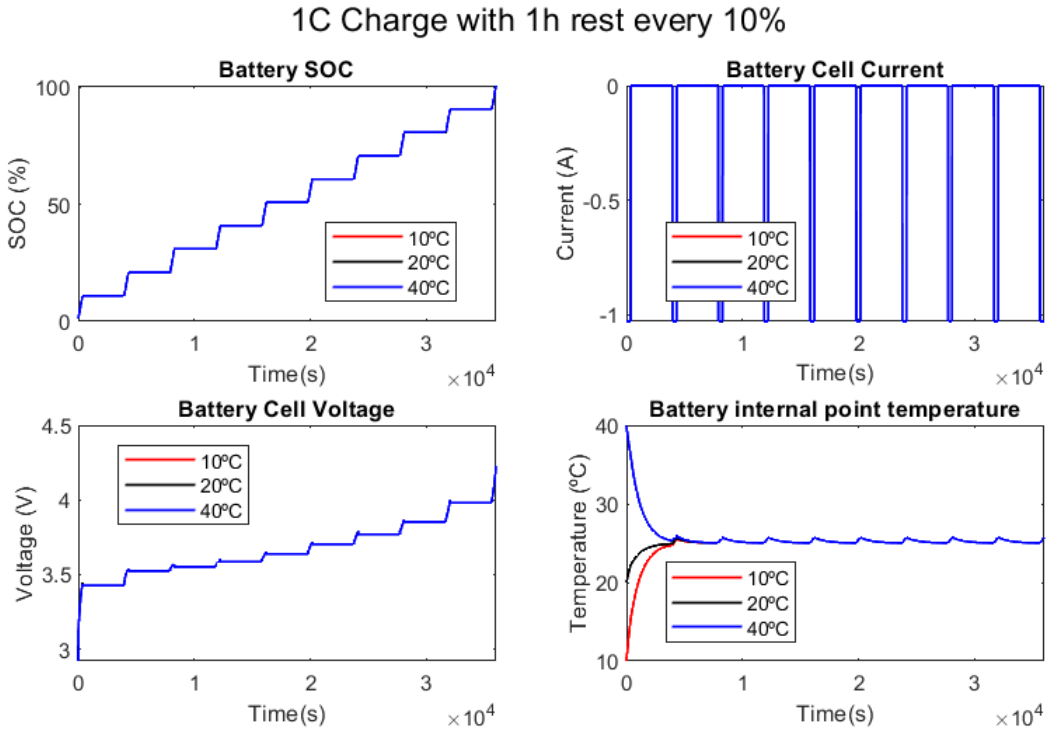

Figure 4.16: SoC, current, voltage, and internal temperature during a 1C charge with a 1 h rest every 10% for initial temperatures of 10 °C, 20 °C and 40 °C.

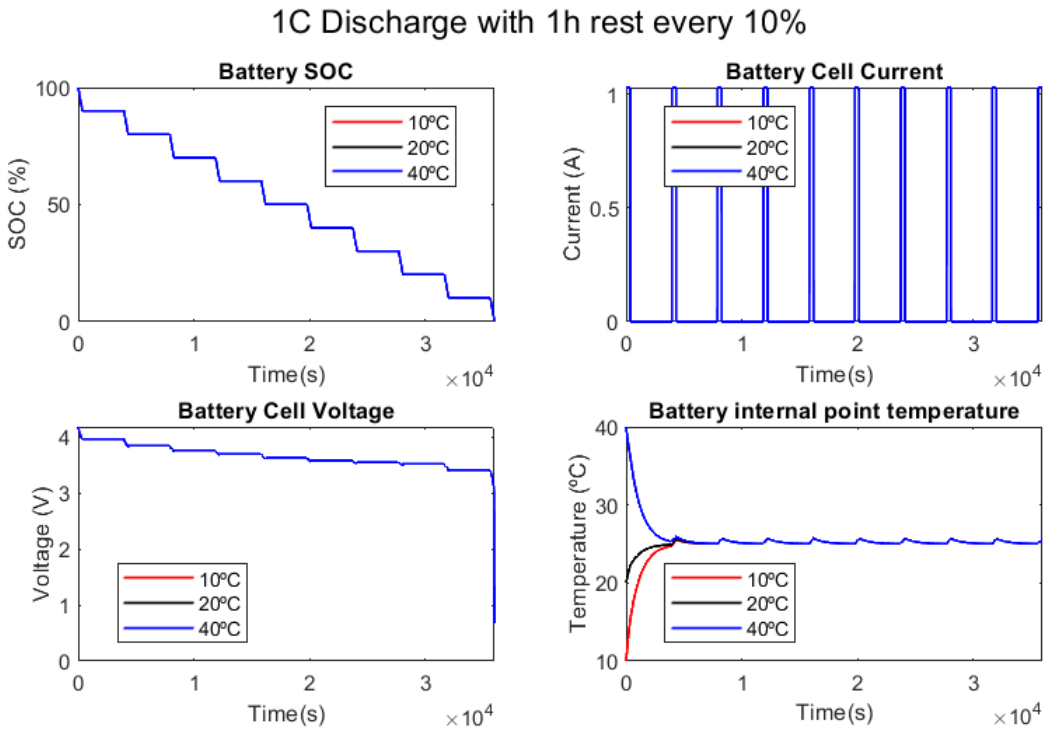

Figure 4.17: SoC, current, voltage, and internal temperature during a 1C discharge with a 1 h rest every 10% for initial temperatures of 10 °C, 20 °C and 40 °C.

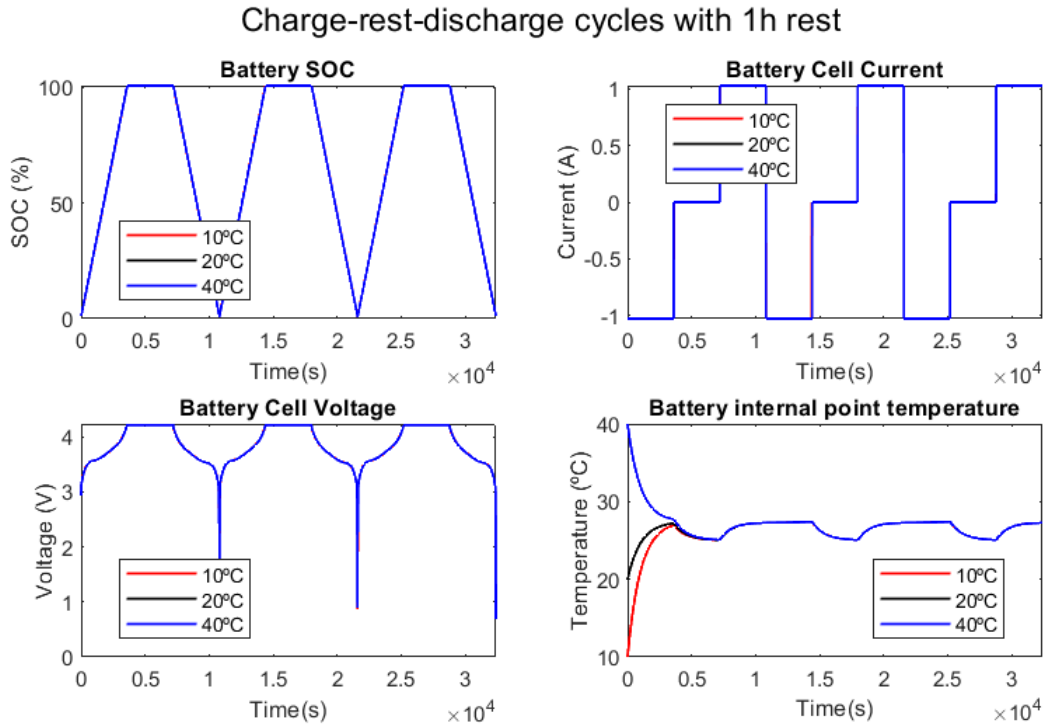

Figure 4.18: SoC, current, voltage, and internal temperature during a 1C charge-rest-discharge with a 1 h rest for initial temperatures of 10 °C, 20 °C and 40 °C.

On Figures 4.16 and 4.17 there are the battery's SoC, current, voltage, and internal point temperature during a 1C charge and discharge with a 1 h rest period every 10%, respectively. On Figure 4.18 there are the same parameters but for cycles of charge, 1 h rest, and discharge. All 3 simulations were made considering initial temperatures of 10 °C, 20 °C and 40 °C.

For all 3 cases, as expected the initial temperature does not influence the behaviour of SoC, voltage and current. For both 10 °C and 20 °C during charge and discharge, the temperature increases at a higher pace (higher for 10 °C) when it's further from the defined ambient temperature of 25 °C. For 40 °C the temperature initially decreases during the procedures. After the temperature first reaches the ambient temperature the behaviour for the 3 cases stops being different. It increases during charge and discharge and decreases to equal the ambient temperature during the rest periods. This happens because during the charge and discharge a load is applied in the battery and its energy causes a heat increase. During rest due to the heat exchange mechanism the battery tends to equal the environment temperature when it reaches the steady state.

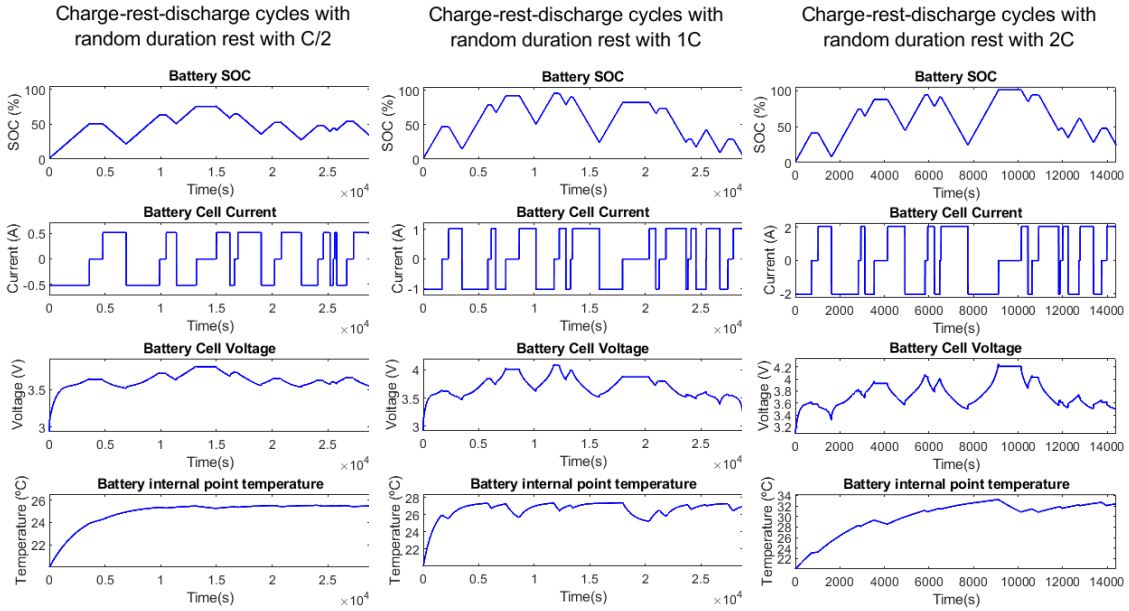

(a) C/2 **(b)** 1C **(c)** 2C

Figure 4.19: SoC, current, voltage, and internal temperature during charge-rest-discharge cycles with random duration.

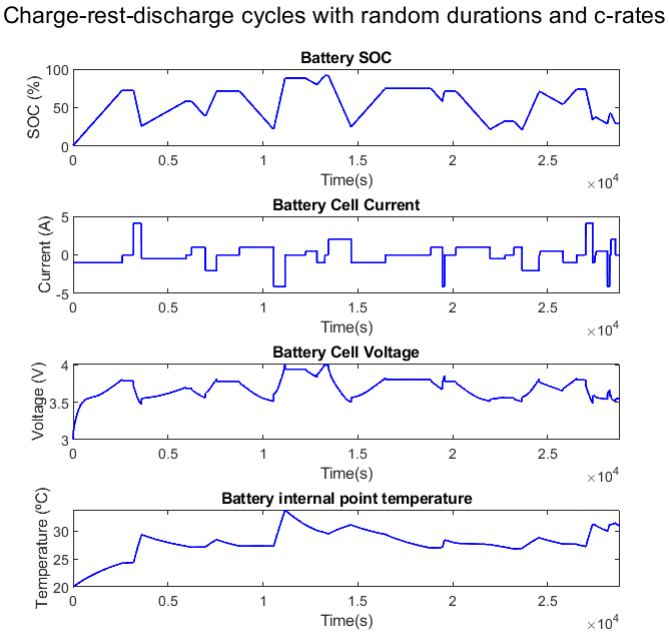

Figure 4.20: SoC, current, voltage, and internal temperature during charge-rest-discharge cycles with random duration and c-rates.

On Figures 4.19a, 4.19b, and 4.19c there are the SoC, current, voltage, and internal temperature behaviour during charge-rest-discharge cycles for C-rates of C/2, 1C, and 2C using random values for the duration of the procedures, respectively.

It is observed the influence the C-rate has on the temperature behaviour. As expected, due to the bigger current value, a higher C-rate (2C and 1C) provides higher temperatures and more noticeable temperature variations than a lower one (C/2). It is also possible to observe that higher c-rates provide higher charging and discharging rates.

On Figure 4.20 the SoC, current, voltage, and internal temperature behaviour during charge-rest-discharge cycles using random duration values and with different C-rates that varied randomly between C/2, 1C, 2C, and 4C. As the previous test, this allowed to see the influence of different C-rates on the battery temperature and charging/discharging rates.

4.2 LIB CYLINDRICAL CELL

In this section will be presented the results for the cylindrical cell simulations. This type of battery was more challenging to model so in a first approach, and as was done with the prismatic cell, simple procedures like full charges and discharges were the way to start. The simulations were made with 1C C-rate and an initial temperature of 20 °C.

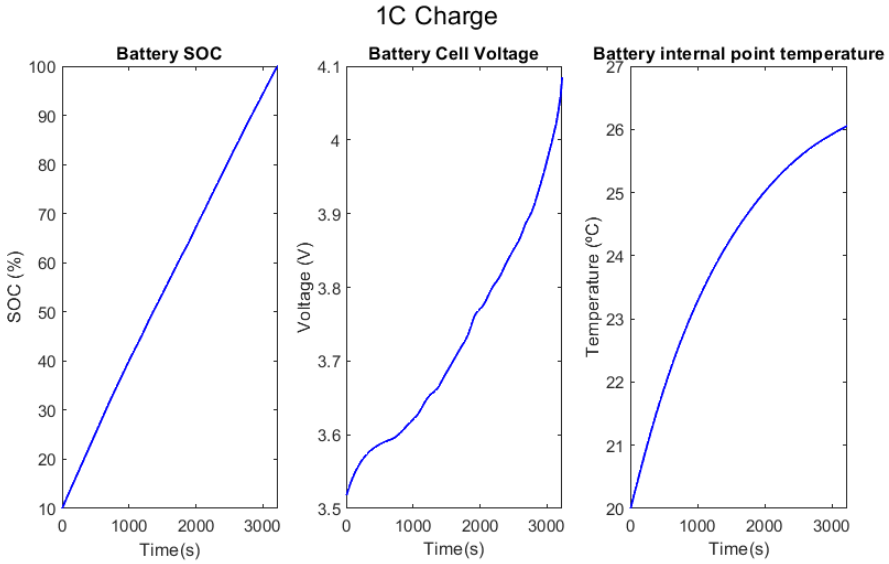

Figure 4.21: SoC, voltage, and internal temperature during a 1C charge cycle.

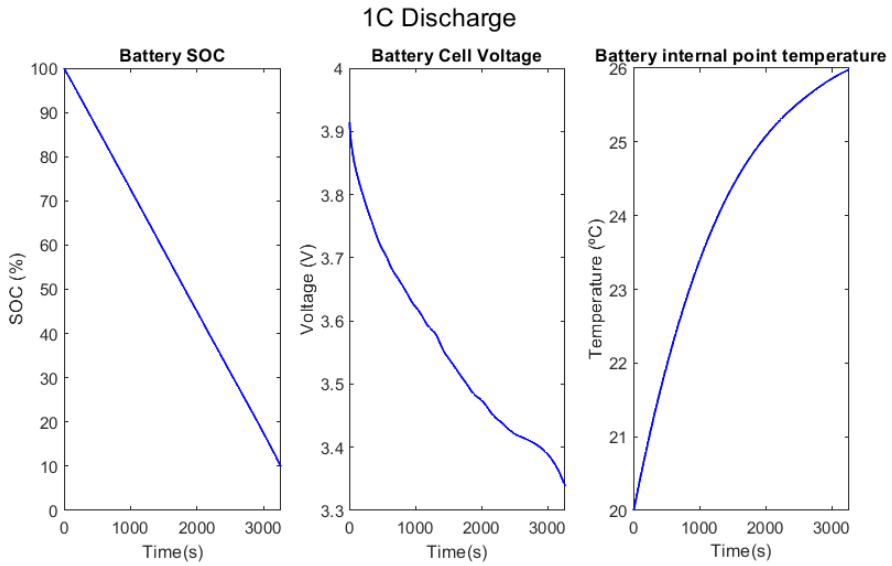

Figure 4.22: SoC, voltage, and internal temperature during a 1C discharge cycle.

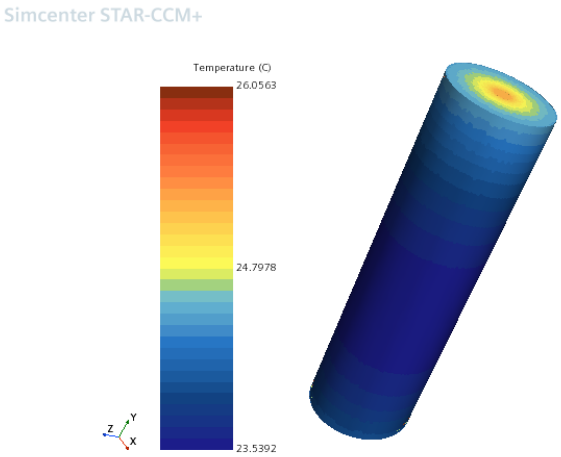

Figure 4.23: Temperature profile of the battery after a 1C charge.

As mentioned, this type of battery was challenging to model, mainly because simulation errors would occur when reaching smaller values of SoC. The errors first happen for higher SoC and with adjustments of the voltage limit values started to happen for smaller values under 10%. For this reason, the lower limit of SoC was limited to 10%: for charge simulations the battery would start at 10% and charge until it was fully charged, and the opposite for discharge simulations. One reason for the error can be the deep discharging of the battery which happens when the cell voltage is bellow the cut-off voltage. As mentioned in chapter 2, although this phenomenon does not cause major safety issues it can cause the battery to stop functioning.

On Figures 4.21 and 4.22 there are the battery's SoC, voltage, and internal point temperature for a 1C charge and discharge cycles, respectively. Both figures show the expected behaviour of the battery: the SoC varies between 10% and 100%, the voltage does not exceed

the defined range of [3.45, 4.2] and the battery temperature increases during the procedure at a higher pace when it's further from the defined ambient temperature of 25 °C.

On Figure 4.23 is shown the temperature profile of the battery after a 1C charge procedure, more precisely the can and positive end plate of the battery. The temperature profile is as expected. Analysing the seen area the temperature is higher near the cathode which is where the current load is applied.

CHAPTER 5

Thermal virtual sensor

In this chapter, a T-BASE algorithm is presented. The results for the prismatic cell presented on chapter 4 are used as input data for the algorithm in order to develop the thermal virtual sensor.

As mentioned in chapter 2, the internal electrochemical behavior of a battery cell during operation genarates internal heat in the battery body which has a direct effect on its thermal dynamics. A common approach to obtain mathematically and via simulation the temperature distribution in a battery is to couple its electrochemical and thermal models. However, the mathematical modelling of the battery electrochemistry, coupled with the thermal dynamics are commonly hard to compute and to implement in onboard applications and a suitable alternative is to use the ECM.

The ECM based on the Thevenin model is useful due to taking in count the nonlinearities of the battery dynamics as the SoC dependence of the electrical parameters [54]. Figure 5.1 shows a scheme of the model.

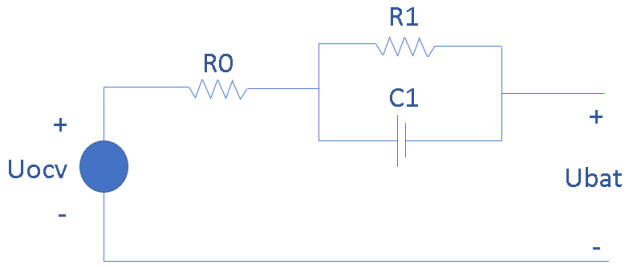

Figure 5.1: Equivalent-circuit model schematic.

By applying the Kirchhoff voltage law, it's possible to obtain the battery open circuit voltage as a function of the voltage on the battery terminal.

$$U_{bat}(t) = U_{OCV}(t) - U_1(t) - R0 \cdot I(t) \tag{5.1}$$

, where $U_{bat}(t)$ is the voltage on the battery terminal, $U_{OCV}(t)$ is the battery Open Circuit Voltage (OCV), $U_1(t)$ is the voltage drop on the impedance 1, R0 is the ohmic internal resistance and $I(t)$ the current on the circuit.

Since a current split occurs in the RC impedance, the total current can be written as the sum of the divided currents:

$$I(t) = C1 \cdot \dot{U}_1(t) + \frac{U_1(t)}{R1} \tag{5.2}$$

Applying the Laplace transform and assuming the system input as the current $I(t)$ and the system output as the difference between the battery OCV and the terminal voltage, the continuous transfer function of the electrical equivalent system is:

$$U_{ocv}(s) - U_{bat}(s)I(s) = \frac{R0 \cdot R1 \cdot C1 \cdot s + (R0 + R1)}{R1 \cdot C1 \cdot s + 1} \tag{5.3}$$

The battery OCV is dependent on how much a battery is charged and may be obtained as function of the battery SoC [55]. An approach is to use experimental data to obtain an interpolation polynomial between OCV and SoC:

$$U_{ocv}(SoC) = \sum_{i=0}^{n} p_i \cdot SoC^n \tag{5.4}$$

Where p_i are the constants of the n-th degree polynomial.

A similar approach can be used to model the thermal behavior of the battery. The thermal resistances and capacitances are related to the material thermal properties such as specific heat and conductivity and geometric characteristics of the battery.

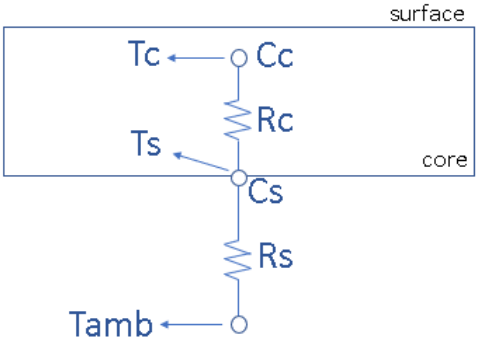

Figure 5.2: Thermal-circuit model schematic.

In figure 5.2 Rc and Cc are the thermal resistance and heat capacity of the battery core and Rs and Cs are the thermal resistance and heat capacity of the battery surface. Assuming a 1D heat transfer and considering an energy balance done on battery core and surface represented by, respectively:

$$C_c \cdot \frac{dT_c(t)}{dt} = \dot{Q} - \frac{T_c(t) - T_s(t)}{R_c} \tag{5.5}$$

$$C_s \cdot \frac{dT_s(t)}{dt} = \frac{T_c(t) - T_s(t)}{R_c} - \frac{T_s(t) - T_{amb}}{R_s} \tag{5.6}$$

Considering the variations $\delta T_s(t)$ and $\delta T_c(t)$ in relation to the ambient temperature, the equations can be reduced to:

$$C_c \cdot \frac{d\delta T_c(t)}{dt} = Q(t) - \frac{\delta T_c(t) - \delta T_s(t)}{R_c} \tag{5.7}$$

$$C_s \cdot \frac{d\delta T_s(t)}{dt} = \frac{\delta T_c(t) - \delta T_s(t)}{R_c} - \frac{\delta T_s(t)}{R_s} \tag{5.8}$$

Applying the Laplace transform and assuming the system input as the heat $Q(t)$ and the system output as the variation of temperature on the battery core, the continuous transfer function of the thermal equivalent system is obtained in:

$$\frac{\delta T_c(s)}{Q(s)} = \frac{Rc \cdot Rs \cdot Cc \cdot s + (Rc + Rs)}{Rc \cdot Rs \cdot Cc \cdot Cs \cdot s^2 + (Rs \cdot Cs + Rs \cdot Cc + Rc \cdot Cc) \cdot s + 1} \tag{5.9}$$

The relation between the thermal and electrical models is given by the heat generation. A formulation for this relation was proposed by [49] and is

$$Q(t) = (U_{ocv}(t) - U_{bat}(t)) \cdot I(t) + I(t) \cdot T_c(t) \cdot \frac{dU_{ocv}(t)}{dT_c(t)} \tag{5.10}$$

The first term on the right side of the equation is the irreversible heat and the second term is the reversible heat as consequence of the entropy change. $\frac{dU_{ocv}(t)}{dT_c(t)}$ is called entropy coefficient. The reversible heat has low influence over the total heat value when compared with the irreversible heat and for this reason can be neglected without prejudice to the results obtained from the models [56].

The transformation of dynamic systems models from continuous to discrete in time domain is a necessary approach for an implementation using digital systems and components. A method used to change representation of a dynamic system in the Laplace domain to the Z domain is applying the Bilinear transformation.

$$s = \frac{2}{\Delta t} \cdot \frac{1 - z^{-1}}{1 + z^{-1}} \tag{5.11}$$

Where Δt is the sampling time.

The Least Squares Method (LSM) is an identification process tool used to estimate numerical values for the parameters of the mathematical model of a dynamic system from the input and output values of a physical experiment [57]. The method minimizes the sum of the squared errors that are the difference between the measured outputs and the estimated outputs

$$J(\theta) = \sum_{i=1}^{k} (Y - \Phi\theta)^2 \tag{5.12}$$

Where Y is the vector containing the measured outputs, Φ is the regressors vector.

To get the minimum value for $J(\theta)$, it is necessary to equal its first derivative to zero. The parameters values are then obtained:

$$\hat{\theta} = \left[\Phi^T \Phi\right]^{-1} \cdot \Phi^T \cdot Y \tag{5.13}$$

Where $\hat{\theta}$ is the vector containing the estimated model parameters. The recursive process of the least squares method is given by:

$$\hat{\theta}(k+1) = \hat{\theta}(k) + \Gamma(k+1) \cdot \left[y(k+1) - \Phi^T(k+1) \cdot \hat{\theta}(k)\right] \tag{5.14}$$

$$\Gamma(k+1) = P(k+1) \cdot \Phi(k+1) \cdot \left[\lambda + \Phi^T(k+1) \cdot P(k) \cdot \Phi(k+1)\right]^{-1} \tag{5.15}$$

$$P(k+1) = \frac{1}{\lambda} \cdot \left[I - \Gamma(k+1) \cdot \Phi^T(k+1)\right] \cdot P(k) \tag{5.16}$$

Where λ is the forgetting factor, $P(k)$ is the covariance matrix and $\Gamma(k)$ is the gain matrix.

The use of an optimized forgetting factor results in an algorithm with lower identification error and faster convergence. The forgetting factor can be updated according to the identification parameter error as shown in [58].

$$\lambda(k) = \lambda_{\min} + (1 - \lambda_{\min}) \cdot h^{\epsilon(k)} \tag{5.17}$$

$$\epsilon(k) = \text{ round } \left(\left(\frac{e(k)}{e_{\text{base}}}\right)^2\right) \tag{5.18}$$

Where $\lambda_{\min}$ is the minimum value of the forgetting factor (usually equals to 0.98), h is the sensitivity coefficient, $e(k)$ is the identification error in the instant k and e_{base} is the allowed error reference. h has commonly the value 0.9 to achieve a balance between rapidity and accuracy of identification parameters.

Relating the discrete model with the parameters obtained from the recursive least squares with the thermal and electrical models after applying the Bilinear Z transform, the resistances and capacitances of the models can be achieved.

One strategy for estimating the core and surface temperatures of a battery cell is to use the Extended Kalman Filter (EKF) approach together with the electrical and thermal models obtained from the identification process. EKF uses a linear approximation in a state space format of a nonlinear process and the measured outputs to estimate the complete vector of states without knowing their initial values. For a nonlinear system, the discrete in time dynamic model is given by

$$x(k) = f_k(x(k-1), u(k), w(k)) \tag{5.19}$$

$$y(k) = h_k(x(k), u(k), v(k)) \tag{5.20}$$

Where $x(k)$ is the system vector of states, $y(k)$ is the system output, $u(k)$ is the system input, $w(k)$ is the process noise and $v(k)$ is the measurement noise.

The EKF recursive equations that make the estimated states converge to the real states are

$$K(k) = P(k) \cdot C^{\wedge}T(k) \cdot C(k) \cdot P(k) \cdot C^{\wedge}T(k) + R(k))^{\wedge} \{-1\} \tag{5.21}$$

$$\hat{x}(k) = \hat{x}(k-1) + K(k) \cdot (y(k) - \hat{y}(k-1)) \tag{5.22}$$

$$P(k) = (I - K(k) \cdot C(k)) \cdot P(k) \tag{5.23}$$

$$\hat{x}(k) = f_k(\hat{x}(k), u(k)) \tag{5.24}$$

$$\hat{y}(k) = h_k(\hat{x}(k), u(k)) \tag{5.25}$$

$$P(k) = A(k) \cdot P(k-1) \cdot A^T(k) + B(k) \cdot Q(k) \cdot B^T(k) \tag{5.26}$$

Where $P(k)$ is the covariance matrix, $K(k)$ is the Kalman gain matrix, $y(k)$ is the measured output, $\hat{y}(k)$ is the estimated output, $\hat{x}(k)$ is the estimated vector of states. For discrete systems $A(k), B(k)$ and $C(k)$ can be defined, respectively, as

$$A(k) = \frac{\partial f_k(x(k-1), u(k))}{\partial x(k)} \tag{5.27}$$

$$B(k) = \frac{\partial f_k(x(k-1), u(k))}{\partial u(k)} \tag{5.28}$$

$$C(k) = \frac{\partial h_k(x(k), u(k))}{\partial x(k)} \tag{5.29}$$

To implement EKF in a digital system, it is necessary to discretize the equations of the electrical and thermal mathematical model. The system can be rewritten as discrete-time equations in

$$U_1(k+1) = \left(1 - \frac{\Delta t}{R_1 \cdot C_1}\right) \cdot U_1(k) + \frac{\Delta t}{C_1} \cdot I(k) \tag{5.30}$$

$$U_{bat}(k) = U_{ocv}(k) - U_1(k) - I(k) \cdot R0 \tag{5.31}$$

$$C_c \cdot \frac{\delta T_c(k+1) - \delta T_c(k)}{\Delta t} = Q(k) - \frac{\delta T_c(k) - \delta T_s(k)}{R_c} \tag{5.32}$$

$$C_s \cdot \frac{\delta T_s(k+1) - \delta T_s(k)}{\Delta t} = \frac{\delta T_c(k+1) - \delta T_s(k)}{R_c} - \frac{\delta T_s(k)}{R_s} \tag{5.33}$$

In addition to estimating the internal and external temperatures, the EKF is intended to also estimate the battery's SoC. For this reason, the SoC has to be one of the states of the states vector and has to be a relation with the system input. The battery's SoC is the ratio of its current capacity to its maximum capacity

$$\mathrm{SoC}(k) = \mathrm{SoC}(k-1) - \frac{I(k) \cdot \delta t}{3600 \cdot C_n} \tag{5.34}$$

Where $I(k)$ is the current in A and C_n is the battery nominal capacity in Ah.

For the proposed EKF the vector of states and the measured output are shown in

$$x(k) = [\mathrm{SoC}(k), U_1(k), T_i(k), T_s(k)] \tag{5.35}$$

$$y(k) = U_{bat}(k) \tag{5.36}$$

Some of the results presented in chapter 4 serve as input data for the estimation algorithm based on the EKF. The tests made are presented on table 4.3.

The discharge tests with 1h of rest between 10 percent of discharge and with external heat transfer by convection were used to obtain the interpolation polynomial with relates the U_{OCV} with the battery SoC. The OCVs were collected for SoC varying from 0.1 to 0.9 and the degree of the used polynomial was equal to 8. Figure 5.3 shows the relation OCV-SoC for the battery simulated in StarCCM+.

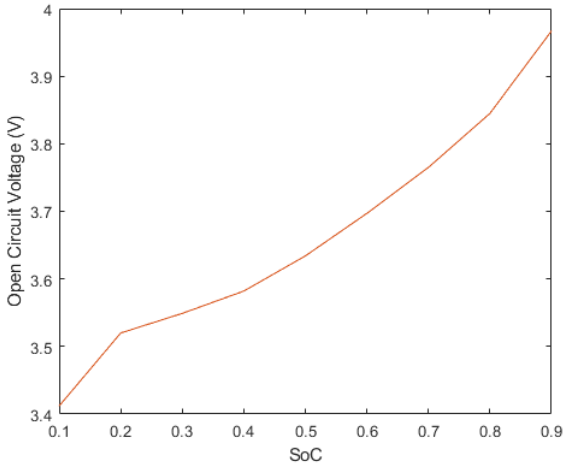

Figure 5.3: Relation OCV-SOC.

The charge tests with 1 h of rest between 10 % of charge and with external convection heat transfer were used to apply the FFRLS method to obtain the parameters for the electrical and thermal models. For the electrical model, the system input was the current and the output was the difference between the OCV, calculated using the polynomial obtained previously, and the voltage. For the thermal model, the system input was the internal generated heat, which was simplified as the product of current and the difference between OCV and voltage, and the output was the difference between the internal temperature and the ambient temperature.

This last approach was considered since the ambient temperature tends to be the equilibrium temperature for the battery and temperature variations due to heating or cooling occur in relation to this temperature. Figures 5.4 and 5.5 represent the outputs of the collected data and the ones estimated with the FFRLS results for the electrical and thermal models, respectively. All of these initial tests were performed with a C-rate equal to 1.

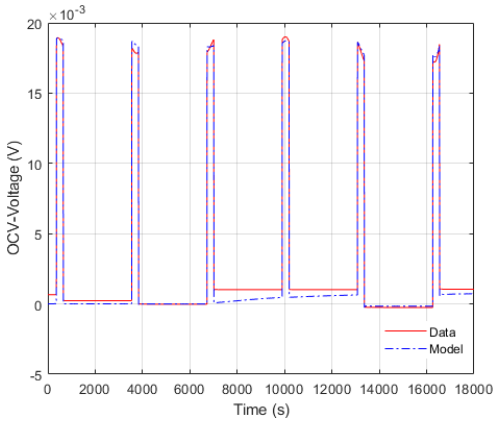

Figure 5.4: OCV-Voltage measured and estimated FFRLS.

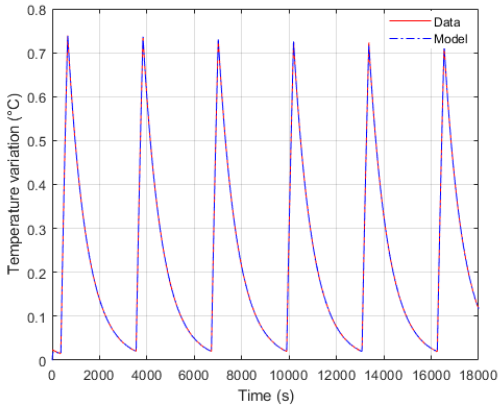

Figure 5.5: Internal temperature measured and estimated FFRLS.

The next step was to test the EKF equations with the simulations with random periods of charge, discharge and rest. Figures 5.6, 5.7, and 5.8 show the behavior of the EKF for the tests performed with C-rates of 1C, 2C and C/2, respectively.

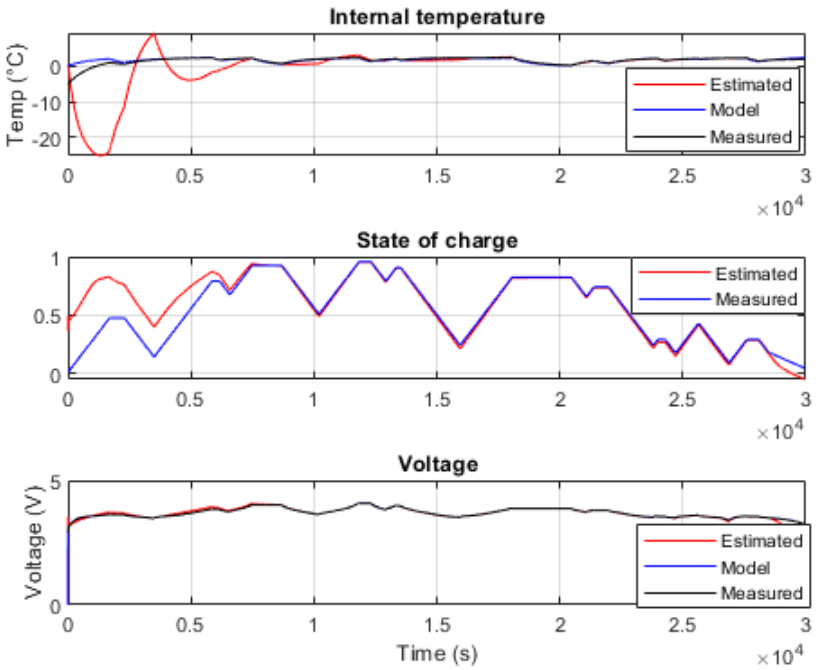

Figure 5.6: Estimations from EKF for tests with 1C.

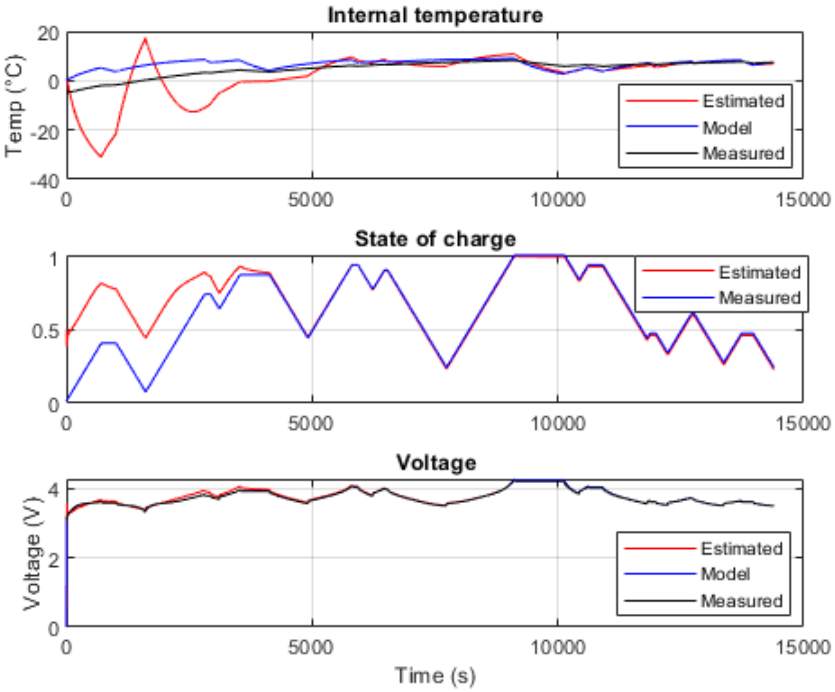

Figure 5.7: Estimations from EKF for tests with 2C.

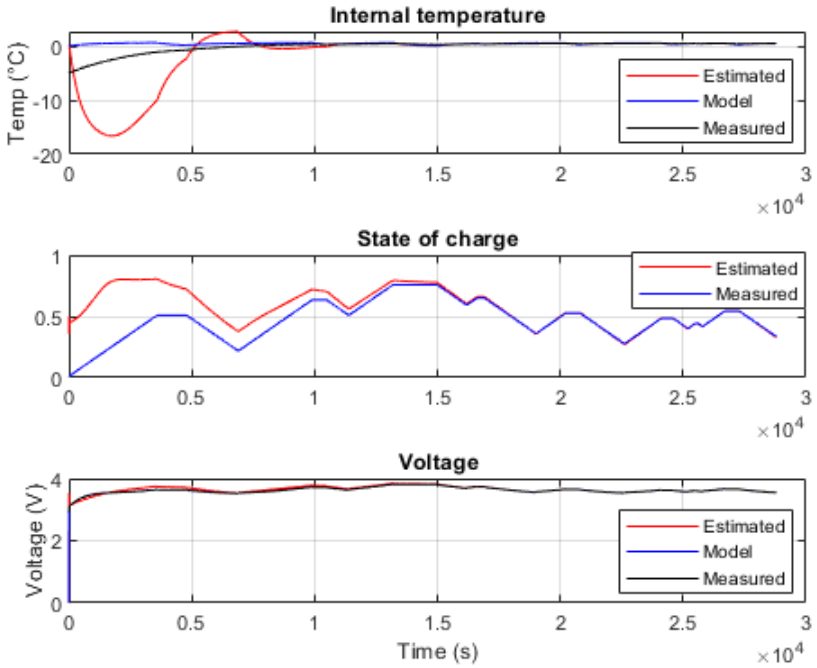

Figure 5.8: Estimations from EKF for tests with C/2 .

It can be seen that even for initial values of SoC, U_1, T_i and T_s different from the real ones, the estimated values tend towards the real ones with time. For all C values, the SoC estimate occurred in a considerably adequate way. It was to be expected that the temperature estimates with this C-rate value would be the best and this was confirmed by the results. The heat generation for higher C-rate values tends to be high and for this reason the temperature

variation tends to be greater. The estimator may not have a good response to this C-rate value due to the large temperature variations around the model's linearization point.

It is important to make it clear that the parameters used for the T-base observer were not the same as those used for the E-base. As the initial approaches to develop the models were made without general knowledge of the real battery characteristics and to ensure that the model could advance to the current stage, there was not much initial concern to guarantee thermal and electrochemical models with the same parameters. However, it is expected to consider this in future versions in order to guarantee the operation of the virtual sensors and to enable evaluations of the existing relationships between the thermal and electrochemical behavior of the cells.

CHAPTER 6

Conclusion

LIB batteries can be used as a way to use more renewable energy sources and consequently reduce the environmental impact. In order to use the batteries safely and efficiently there is a need to monitor their status and predict their behaviour. Battery modelling can be an helpful tool to help accomplish this goal. Due to its complexity, 3D computation and softwares like the BDS and StarCCM+ are required to obtain better results.

Regarding battery modelling there are multiple types of models to choose from, including the NTGP and RCR model. When compared to the given experimental results, the NTGP proved to be the most adequate to model the prismatic LIB cell. It was also seen the influence of the boundary condition and the importance of considering heat transfer mechanisms. The lack of these aspects can provide unrealistic results. The other tests made for this cell allowed to see the influence of the C-rate and initial temperature on the cell behaviour, especially in the temperature.

Regarding the cylindrical LIB cell despite the deep discharging issue, the behaviour of the battery was the expected.

The obtained data proved to be helpful in the development of the thermal virtual sensor. The results of the preformed tests were used as input data for the estimation algorithm based on EKF presented in chapter 5 which provided good results: for all C-rate values the temperature and SoC estimate occurred in a considerably adequate time.

Despite being challenging softwares to work with BDS and StarCCM+ have their advantages. The results and their application show that they can be considered reliable softwares to model and study multiple types of LIB cells.

Model optimization is always something to improve. A suggestion for future work is to better define the convection heat exchange constant for different environments and battery positions in order to optimize the results.

Another obvious step for future work would be to solve the cylindrical cell simulation issue with deep discharging to model full charge and discharge procedure. After that, the same type of tests that were made for the prismatic cell would be made in order to adapt the

thermal virtual sensor to other type of cells.

Regarding the virtual sensor, there will be more concern to guarantee thermal and electrochemical models with the same parameters. Additionally, experimental tests on both prismatic and cylindrical cells are being performed to corroborate the simulations results. Both these aspects will allow further optimization and development of the sensor.

References

[1] R. Farreny, X. Gabarrell, and J. Rieradevall, "Energy intensity and greenhouse gas emission of a purchase in the retail park service sector: An integrative approach," *Energy policy*, vol. 36, no. 6, pp. 1957–1968, 2008.

[2] "Final energy comsumption by sector," [Online; accessed 7-October-2022]. [Online]. Available: https://ec.europa.eu/eurostat/databrowser/view/ten00124/default/line?lang=en.

[3] E. E. Agency, *Primary and final energy consumption in europe*, https://www.eea.europa.eu/ims/primary-and-final-energy-consumption, [Online; accessed 6-July-2022], Mar. 2022.

[4] ——, *Final energy consumption by sector and fuel in europe*, https://www.eea.europa.eu/data-and-maps/indicators/final-energy-consumption-by-sector-10/assessment, [Online; accessed 19-July-2022], Jan. 2020.

[5] J. Rogelj, M. Den Elzen, N. Höhne, *et al.*, "Paris agreement climate proposals need a boost to keep warming well below 2 c," *Nature*, vol. 534, no. 7609, pp. 631–639, 2016.

[6] B. 2. large-scale research initiative, *Battery2030+*, https://battery2030.eu/, [Online; accessed 6-July-2022], Jan. 2021.

[7] V. Etacheri, R. Marom, R. Elazari, G. Salitra, and D. Aurbach, "Challenges in the development of advanced li-ion batteries: A review," *Energy & Environmental Science*, vol. 4, no. 9, pp. 3243–3262, 2011.

[8] J. Huang, X. Han, F. Liu, *et al.*, "Monitoring battery electrolyte chemistry via in-operando tilted fiber bragg grating sensors," *Energy & Environmental Science*, vol. 14, no. 12, pp. 6464–6475, 2021.

[9] Instabat, *Instabat project - based on battery 2030+ group*, https://www.instabat.eu/, [Online; accessed 20-July-2022], Mar. 2021.

[10] L. Liu, S. M. Kuo, and M. Zhou, "Virtual sensing techniques and their applications," in *2009 International Conference on Networking, Sensing and Control*, IEEE, 2009, pp. 31–36.

[11] M. Nascimento, M. S. Ferreira, and J. L. Pinto, "Temperature fiber sensing of li-ion batteries under different environmental and operating conditions," *Applied Thermal Engineering*, vol. 149, pp. 1236–1243, 2019.

[12] R. Modirnia, *Modeling, advanced temperature measurement, and control algorithms in thermoforming*. McGill University (Canada), 2016.

[13] M. Charkhgard and M. Farrokhi, "State-of-charge estimation for lithium-ion batteries using neural networks and ekf," *IEEE Transactions on Industrial Electronics*, vol. 57, no. 12, pp. 4178–4187, 2010. DOI: 10.1109/TIE.2010.2043035.

[14] H. Rahimi-Eichi, F. Baronti, and M.-Y. Chow, "Online adaptive parameter identification and state-of-charge coestimation for lithium-polymer battery cells," *IEEE Transactions on Industrial Electronics*, vol. 61, no. 4, pp. 2053–2061, 2014. DOI: 10.1109/TIE.2013.2263774.

[15] F. Auger, M. Hilairet, J. M. Guerrero, E. Monmasson, T. Orlowska-Kowalska, and S. Katsura, "Industrial applications of the kalman filter: A review," *IEEE Transactions on Industrial Electronics*, vol. 60, no. 12, pp. 5458–5471, 2013. DOI: 10.1109/TIE.2012.2236994.

[16] E. Gümüşsu, Ö. Ekici, and M. Köksal, "3-d cfd modeling and experimental testing of thermal behavior of a li-ion battery," *Applied Thermal Engineering*, vol. 120, pp. 484–495, 2017.

[17] A. Samba, "Battery electrical vehicles-analysis of thermal modelling and thermal management," Ph.D. dissertation, LUSAC (Laboratoire Universitaire des Sciences Appliquées de Cherbourg . . ., 2015.

[18] A. C. Urbano, "Electro thermal modeling of lithium-ion batteries," 2016.

[19] H. Budde-Meiwes, J. Drillkens, B. Lunz, *et al.*, "A review of current automotive battery technology and future prospects," *Proceedings of the Institution of Mechanical Engineers, Part D: Journal of Automobile Engineering*, vol. 227, pp. 761–776, May 2013. DOI: 10.1177/0954407013485567.

[20] M.-T. Von Srbik, "Advanced lithium-ion battery modelling for automotive applications," 2015.

[21] D. Zapata Dominguez, "Investigation of the cycling mechanisms in silicon and germanium-based lithium-ion batteries by ex-situ and operando x-ray scattering techniques," Ph.D. dissertation, Dec. 2020.

[22] J. Salminen, T. Kallio, N. Omar, P. Van den Bossche, J. Van Mierlo, and H. Gualous, "Transport energy–lithium ion batteries," in *Future Energy*, Elsevier, 2014, pp. 291–309.

[23] B. Xu, D. Qian, Z. Wang, and Y. S. Meng, "Recent progress in cathode materials research for advanced lithium ion batteries," *Materials Science and Engineering: R: Reports*, vol. 73, no. 5-6, pp. 51–65, 2012.

[24] C. De las Casas and W. Li, "A review of application of carbon nanotubes for lithium ion battery anode material," *Journal of Power Sources*, vol. 208, pp. 74–85, 2012.

[25] J. B. Goodenough and Y. Kim, "Challenges for rechargeable batteries," *Journal of Power Sources*, vol. 196, no. 16, pp. 6688–6694, 2011.

[26] T.-F. Yi, L.-J. Jiang, J. Shu, C.-B. Yue, R.-S. Zhu, and H.-B. Qiao, "Recent development and application of li4ti5o12 as anode material of lithium ion battery," *Journal of Physics and Chemistry of Solids*, vol. 71, no. 9, pp. 1236–1242, 2010.

[27] P. Kubiak, J. Geserick, N. Hüsing, and M. Wohlfahrt-Mehrens, "Electrochemical performance of mesoporous tio2 anatase," *Journal of Power Sources*, vol. 175, no. 1, pp. 510–516, 2008.

[28] K. Zaghib, J. Dubé, A. Dallaire, *et al.*, "Lithium-ion cell components and their effect on high-power battery safety," in *Lithium-Ion Batteries*, Elsevier, 2014, pp. 437–460.

[29] C. F. Francis, I. L. Kyratzis, and A. S. Best, "Lithium-ion battery separators for ionic-liquid electrolytes: A review," *Advanced Materials*, vol. 32, no. 18, p. 1 904 205, 2020.

[30] Q. Wang, P. Ping, X. Zhao, G. Chu, J. Sun, and C. Chen, "Thermal runaway caused fire and explosion of lithium ion battery," *Journal of power sources*, vol. 208, pp. 210–224, 2012.

[31] C.-Y. Jhu, Y.-W. Wang, C.-M. Shu, J.-C. Chang, and H.-C. Wu, "Thermal explosion hazards on 18650 lithium ion batteries with a vsp2 adiabatic calorimeter," *Journal of hazardous materials*, vol. 192, no. 1, pp. 99–107, 2011.

[32] G.-H. Kim, A. Pesaran, and R. Spotnitz, "A three-dimensional thermal abuse model for lithium-ion cells," *Journal of power sources*, vol. 170, no. 2, pp. 476–489, 2007.

[33] L. Lu, X. Han, J. Li, J. Hua, and M. Ouyang, "A review on the key issues for lithium-ion battery management in electric vehicles," *Journal of power sources*, vol. 226, pp. 272–288, 2013.

[34] T. B. Reddy, *Linden's handbook of batteries*. Mcgraw-hill New York, 2011, vol. 4.

[35] N. Omar, M. A. Monem, Y. Firouz, *et al.*, "Lithium iron phosphate based battery–assessment of the aging parameters and development of cycle life model," *Applied Energy*, vol. 113, pp. 1575–1585, 2014.

[36] A. Barré, B. Deguilhem, S. Grolleau, M. Gérard, F. Suard, and D. Riu, "A review on lithium-ion battery ageing mechanisms and estimations for automotive applications," *Journal of Power Sources*, vol. 241, pp. 680–689, 2013.

[37] K. E. Thomas, J. Newman, and R. M. Darling, "Mathematical modeling of lithium batteries," in *Advances in lithium-ion batteries*, Springer, 2002, pp. 345–392.

[38] H. E. Perez, *Model based optimal control, estimation, and validation of lithium-ion batteries*. University of California, Berkeley, 2016.

[39] H. Gu, "Mathematical analysis of a zn/niooh cell," *Journal of the Electrochemical Society*, vol. 130, no. 7, p. 1459, 1983.

[40] U. S. Kim, C. B. Shin, and C.-S. Kim, "Modeling for the scale-up of a lithium-ion polymer battery," *Journal of Power Sources*, vol. 189, no. 1, pp. 841–846, 2009.

[41] J. Newman and W. Tiedemann, "Potential and current distribution in electrochemical cells: Interpretation of the half-cell voltage measurements as a function of reference-electrode location," *Journal of The Electrochemical Society*, vol. 140, no. 7, p. 1961, 1993.

[42] W. Wu, S. Wang, W. Wu, K. Chen, S. Hong, and Y. Lai, "A critical review of battery thermal performance and liquid based battery thermal management," *Energy conversion and management*, vol. 182, pp. 262–281, 2019.

[43] S. Barcellona and L. Piegari, "Integrated electro-thermal model for pouch lithium ion batteries," *Mathematics and Computers in Simulation*, vol. 183, pp. 5–19, 2021.

[44] M. Nikdel *et al.*, "Various battery models for various simulation studies and applications," *Renewable and Sustainable Energy Reviews*, vol. 32, pp. 477–485, 2014.

[45] M. Verbrugge and E. Tate, "Adaptive state of charge algorithm for nickel metal hydride batteries including hysteresis phenomena," *Journal of Power Sources*, vol. 126, no. 1-2, pp. 236–249, 2004.

[46] S. Wang, M. Verbrugge, J. S. Wang, and P. Liu, "Power prediction from a battery state estimator that incorporates diffusion resistance," *Journal of Power Sources*, vol. 214, pp. 399–406, 2012.

[47] C. R. Pals and J. Newman, "Thermal modeling of the lithium/polymer battery: I. discharge behavior of a single cell," *Journal of the Electrochemical Society*, vol. 142, no. 10, p. 3274, 1995.

[48] ——, "Thermal modeling of the lithium/polymer battery: Ii. temperature profiles in a cell stack," *Journal of the Electrochemical Society*, vol. 142, no. 10, p. 3282, 1995.

[49] D. Bernardi, E. Pawlikowski, and J. Newman, "A general energy balance for battery systems," *Journal of the electrochemical society*, vol. 132, no. 1, p. 5, 1985.

[50] G. G. Botte, V. R. Subramanian, and R. E. White, "Mathematical modeling of secondary lithium batteries," *Electrochimica Acta*, vol. 45, no. 15-16, pp. 2595–2609, 2000.

[51] B. Shabani and M. Biju, "Theoretical modelling methods for thermal management of batteries," *Energies*, vol. 8, no. 9, pp. 10 153–10 177, 2015.

[52] D. T. R. Eswarawaka, "Effect of geometrical size and unit cell capacity on high performance lithium-ion battery," 2016.

[53] F. Freitas, "Desenvolvimento de sensores em fibra ótica para avaliação do desempenho e segurança de baterias de iões de lítio," M.S. thesis, University of Aveiro, 2022.

[54] M. Mohamed, H. Ahmad, M. A. Seman, S. Razali, and M. Najib, "Electrical circuit model of a vanadium redox flow battery using extended kalman filter," *Journal of Power Sources*, vol. 239, pp. 284–293, 2013.

[55] H. Pang, L. Guo, L. Wu, J. Jin, F. Zhang, and K. Liu, "A novel extended kalman filter-based battery internal and surface temperature estimation based on an improved electro-thermal model," *Journal of Energy Storage*, vol. 41, p. 102 854, 2021.

[56] C. Forgez, D. V. Do, G. Friedrich, M. Morcrette, and C. Delacourt, "Thermal modeling of a cylindrical lifepo4/graphite lithium-ion battery," *Journal of Power Sources*, vol. 195, no. 9, pp. 2961–2968, 2010.

[57] H. Pang, L. Guo, L. Wu, and X. Jin, "An enhanced temperature-dependent model and state-of-charge estimation for a li-ion battery using extended kalman filter," *International Journal of Energy Research*, vol. 44, no. 9, pp. 7254–7267, 2020.

[58] X. Sun, J. Ji, B. Ren, C. Xie, and D. Yan, "Adaptive forgetting factor recursive least square algorithm for online identification of equivalent circuit model parameters of a lithium-ion battery," *Energies*, vol. 12, no. 12, p. 2242, 2019.